A Finite Element Analysis of Room Temperature Silicon Crystals for the Advanced Photon Source Bending Magnet and Insertion Device Beams

Lahsen Assoufid, Wah-Keat Lee, and Dennis M. Mills

Contents

A Finite Element Analysis of Room Temperature Silicon Crystals
for the Advanced Photon Source
Bending Magnet and Insertion Device Beams

Lahsen Assoufid, Wah-Keat Lee, and Dennis M. Mills

Abstract

The third generation of synchrotron radiation sources, such as the Advanced Photon Source (APS), will provide users with a high brilliance x-ray beam with high power and power densities. In many cases, the first optical component to intercept the x-ray beam is a silicon-crystal monochromator. Due to extreme heat loading, the photon throughput and brilliance will be severely degraded if the monochromator is not properly designed (or cooled). This document describes a series of finite element analyses performed on room temperature silicon for the three standard APS sources, namely, the bending magnet, wiggler A, and undulator A. The modeling is performed with the silicon cooled directly with water or liquid gallium through rectangular channels. The temperature distributions and thermally induced deformations are presented.

I. Introduction

The Advanced Photon Source (APS) will provide researchers with x-ray beams of unparalleled brilliance. Concomitant with this increase in brilliance is a substantial increase in the total power and power density compared to those from existing sources. The APS has put considerable effort into exploring various approaches to mitigate the thermal distortion problem in x-ray optical components. In particular, for double-crystal monochromators, the use of silicon cooled with liquid gallium [1-3], silicon at cryogenic temperatures [4-5], the effect of crystal geometry (inclined [6-12], asymmetric [13], and thin crystals), and the use of diamond [14-15] instead of silicon are all being studied both experimentally and computationally. This document summarized a series of finite element analyses (FEA) performed on room temperature silicon for the three standard APS source, namely, a bending magnet, wiggler A, and undulator A. All modeling is performed with the silicon directly cooled with water or liquid gallium through rectangular channels. The temperature distribution and the maximum thermally induced deformations are presented. In all cases, we assume the monochromator to be the first optical component in the beamline. Obviously any arrangement, such as inclusion of a mirror as the first optical component, that reduces the power density and the total power incident on the crystal will improve its performance, albeit in some cases by transferring the thermal problem from one component to another. Clearly not every experimental configuration could be modeled, and so we present these findings as a starting point or guide for users in the design of the first optical components for their particular program requirements.

II. Parameters Used for FEA Calculations

All thermal and structural analyses were performed using version 5.0a of the ANSYS code [16].

1) The heat transfer coefficient

The heat transfer coefficient, h(T), is calculated using the following equation:

$$h(T) = \frac{Nuk(T)}{D_h},$$

(1)

where Nu is the Nusselt number, D_h is the hydraulic diameter, and k is the thermal conductivity of the coolant.

For liquid gallium, the Lyon equation was used [17]:

$$Nu = 7.0 + 0.025 R_e^{0.8} P_r^{0.8}$$

(2)

For water, the Gnielinski equation (valid for Reynolds numbers 2300) was used [18]:

$$Nu = \frac{(R_e - 1000) P_r f / 2}{1.0 + 12.7(P_r^{2/3} - 1)\sqrt{f/2}}.$$

(3)

R_e (= vD_h/μ) is the Reynolds number, with v the coolant velocity; μ and are the coolant dynamic viscosity and density, respectively, and D_h is the hydraulic diameter; P_r (=$C_p\mu/k$) is the Prandlt number, with C_p the coolant heat capacity; f is the friction coefficient and is given by the following formula [19]:

$$f = \{1.58\ln(R_e) - 3.28\}^{-2}.$$

(4)

The hydraulic diameter for rectangular channels can be evaluated using the following equation:

$$D_h = \frac{2wh}{w + h},$$

(5)

where w and h are the channel width and height, respectively.

2) Materials properties

Some of the relevant thermophysical properties of silicon (at 20°C) and liquid gallium (at 50°C) are listed in Table 1. Figs II.1a and b show the variation of the thermal conductivity and of the coefficient of thermal expansion of silicon as a function of temperature [20].

Table 1. Properties of silicon (at 20°C) and liquid gallium (at 50°C).

Property	Silicon	Liquid Gallium
Thermal conductivity (W/cm-°C)	1.256	0.30
Density (kg/m^3)	2330	6090
Specific heat (J/kg-K)	754	343
Thermal coefficient of expansion (/°C)	2.33×10^{-6}	NA
Dynamic viscosity (N s/m^2)	NA	1.7×10^{-3}
Young's modulus (GPa)	167.4	NA
Poisson's ratio	0.25	NA

(a)
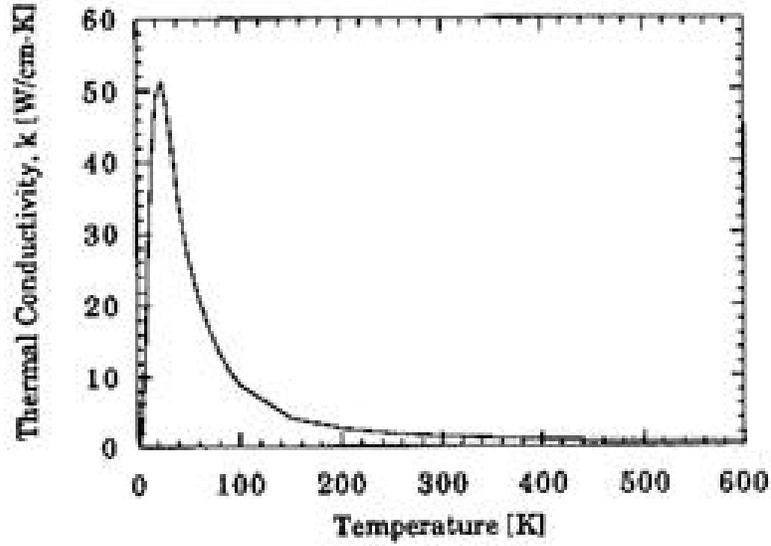
(b)
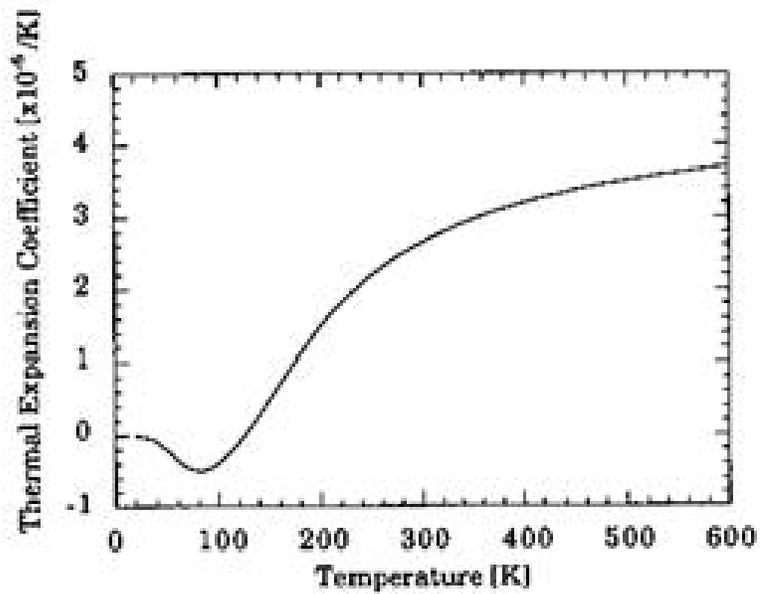
Fig. II.1: (a) Thermal conductivity, and (b) expansion coefficient of silicon as a function of temperature (data taken from Ref. 20).

III. The Bending Magnet Monochromator

A. Properties of the source

1. Source parameters

The bending magnet source parameters are summarized in Table 2 [21]:

Table 2. Bending Magnet Source Parameters

Parameter	Value
Ring energy, E_r [GeV]	7.0
Positron beam current, I [mA]	100.0
Radius, r [m]	38.96
Magnetic field, B [T]	0.599
Critical energy, E_c [keV]	19.5
Flux at E_c [phot/s $\cdot$ 0.1% BW $\cdot$ mrad]	1.12×10^{13}
Horizontal size, $_x$ [mm]	0.114
Vertical size, $_y$ [mm]	0.111
1 / [μrad]	73
Power [watts/mradH-mA]	0.87

2. Total power, heat flux, and source spectrum

At a ring energy of 7 GeV and a current of 100 mA, the bending magnet (BM) will radiate a total power of 86.7 watts per horizontal milliradian. The front-end components of the APS BM beamline were designed so that only 6 mrad of the beam will be accepted. Hence, the total accepted power is about 520 watts. With an APS Be window assembly (two 0.250-mm-thick beryllium windows), the peak normal heat flux at 30 m from the source is about 0.82 W/mm^2. Fig. III.1 shows the source spectral power for 1 mA current, integrated over the vertical angle. The two Be windows absorb about 0.110 W/mradH-mA. Fig. III.2 gives the power density profile in the vertical direction at normal incidence at 30 m, the monochromator location.

B. Description and analyses of the crystal

1. Crystal geometry and coolant parameters

The crystal geometry is sketched in Fig. III.3. It is directly cooled by flowing water through 51 rectangular channels. Each channel is 1 mm wide and 5 mm deep. The depth of 5 mm was chosen to keep the fin efficiency at a reasonable value and, at the same time, to maintain the water flow in a turbulent regime. The fins are also 1 mm thick each, and the base of the crystal was chosen so that it is thick enough (30 mm) to minimize the bowing of the crystal under the thermal load.

The distortions on the crystal surface are mainly determined by the amount of power deposited in the face plate. Therefore, to minimize the x-ray absorption, the face plate must be chosen to be as thin as possible. However, both the pressure-induced deformation and the fabrication aspects have to be considered. We found that a 0.5-mm-thick face plate is a good compromise (doubling the thickness will double the thermally induced slope error).

It has been seen both experimentally and computationally [22] that the periodicity of the channels and the fins results in a periodic variation of the temperature profile on the crystal surface, across the channels. This periodic variation of the temperature might eventually lead to a periodic slope error variation superimposed on the overall slope error due to the temperature gradient across the beam footprint. To avoid having this slope error structure in the tangential direction, the channels are oriented along the beam direction. However, the magnitude of this effect depends on the power load, the channel and fin geometry, the crystal face plate thickness, and the heat transfer coefficient.

The overall size of the crystal is 120 mm x 102 mm x 35.5 mm, and this size is maintained throughout the analyses. However, because the BM power profile is uniform in the horizontal direction, only half of a channel-cell (see Fig. III.3) was used as a model in the finite element analysis. After comparison with a full crystal model, it was found that this assumption leads to slightly conservative results. However, the computation time is significantly reduced, and the error in terms of maximum slope error (which is the parameter we want to evaluate) is on the order of 15%.

Because the magnitude of the power and power density emitted by the bending magnet is low, water cooling is sufficient. For our analyses, we have chosen a flow rate of 5.5 gpm, flowing in 51 channels, which corresponds to a fluid velocity of about 1.39 m/s and a Reynolds number of about 2700. The heat transfer coefficient estimated using equations (1) and (3) is about 0.61 W/cm^2-K. The coolant average temperature is set to 25°C, and its temperature rise along the channels is estimated to be on the order of 0.3°C.

2. Power load and boundary conditions

As mentioned previously, because the BM power profile is uniform in the horizontal direction, only half of a channel-cell was used to model the crystal. The absorbed power along the beam optical path is evaluated using PHOTON2 [23] by dividing the crystal into several layers and calculating the power density profile absorbed by each layer. Fig. III.4 shows the variation of the absorbed power density by a silicon crystal under the bending magnet beam, as a function of thickness. Calculations show that, for a Si(111) crystal set to diffract 4-keV photons, about 54% of the incident power is absorbed in the 0.5-mm-thick face plate. The remaining power (i.e., the fraction that is not reflected from the crystal surface or transmitted through the crystal base) is distributed between the fins, the coolant, and the base. The total absorbed power depends on the length of the optical path of the beam within the crystal, which depends on the Bragg angle and the crystal size.

The absorbed power is treated as a heat generation rate in the thermal analysis and is used to evaluate the temperature distribution and the corresponding distortion field. In all our calculations, the silicon is assumed to be isotropic, and the material properties are evaluated as a function of temperature. For the structural boundary conditions, the crystal is held at the center node (i.e., at x=0, y=0, z=0, see Fig. III.3), and, in order to avoid crystal rotation around the x-axis, the opposite node on the bottom face is restrained in the z-direction. Finally, the channel midplane is at the crystal plane of symmetry, and, in order to take into account the effect of the adjacent channels, all the nodes at the fin midplane are restrained in the x-direction.

C. Temperature and distortion results

The performance of the crystal was studied for x-ray energies from 4 to 24 keV. The thermal and structural results are summarized in Table 3. For comparison, the Darwin width for the symmetric Si(111) reflection for each energy is also given. Fig. III.5 shows the isotherms for a Si(111) crystal set to diffract 4-keV photons (Bragg angle=29.6°). Fig. III.6 shows the displacement and slope error profile along the center line of a Si(111) set to diffract 4-keV photons. Note that a 30-mm-thick base was enough to reduce the bowing component to a minimum (the slope profile goes back to zero at the edges of the crystal). The crystal distortion profile is, therefore, mainly due to the temperature distribution on the crystal surface. At 4 keV, which corresponds to the highest heat flux, the increase in temperature above that of the coolant (25°C) is about 7.5°C, and the total thermally induced slope error is only about 26% of the Darwin width. At higher photon energies (lower incidence angles), although the surface power density is lower, the total absorbed power is much higher due to the increased optical path as the beam traverses the crystal. This impacts on the thermally induced slope errors: at 8 keV (Bragg angle = 14.3°), the thermally induced slope error is 32% of Darwin width, while at 24 keV (Bragg angle = 4.7°), it is equal to 40%. However, at high photon energies, one can certainly improve the crystal performance by using appropriate filters to cut off all the power from lower energy x-rays, which would be otherwise absorbed in the face plate.

Finally, remember that the above analyses are based on a crystal with a cooled area that is 102 mm wide (51 channels). Reducing the width of the crystal will increase the fluid velocity (fewer

channels), and accordingly it increase the heat transfer coefficient for the fixed flow rate of 5.5 gpm. As an example, calculations were performed for a 62-mm crystal (29 channels and about 2-mrad horizontal beam opening). For the 4-keV case, the thermally induced slope error is reduced to about 17% of the Darwin width, while at 24 keV it is reduced to about 23%. Fig. III.7 shows the variation of the thermally induced slope error as a function of Bragg's angle for both cases.

D. Conclusion

Our simulations show that a water-cooled Si(111) slotted crystal will perform acceptably under the heat load form the APS bending magnet beam. The effective slope error for the 4-keV case, which corresponds to the highest heat flux on the crystal surface, is only about 26% of the Darwin width. For higher energies, the ratio of the total slope error to the Darwin width is larger due to the increase in the power absorbed by the face plate (lower incidence angle) along with the decrease of the Darwin width. However, in this case, one can certainly further reduce the distortions by using appropriate filters to cut off the power load form lower energy x-rays.

The modeled crystal was wide enough (102 mm) to intercept about 3.4 mrad of the horizontal beam opening. If a smaller crystal was ;used with the same flow rate, much higher fluid velocities, and hence better heat transfer properties could be obtained. As an example, we performed the analysis for a 62-mm-wide crystal; the thermally induced slope errors were reduced by 35 to 45% compared to the case of the 102-mm crystal (see Fig. III.7). The same performance can be achieved by simply increasing the flow rate. However, the increase in the fluid velocity may be limited because of the flow-induced vibrations. In the extreme case, further improvement can be obtained by using liquid gallium as a coolant instead of water. Liquid gallium gives much higher heat transfer coefficients for a fixed flow rate compared to water. With water as a coolant, enhance heat exchangers, such as the pin-post [24], microchannel design [25-26], or cooling channels filled with porous medium [27], should also be considered.

Finally, the analysis is conservative in the sense that all the power lost from the incident beam is converted into heat. No attempt was made to consider losses form Compton scattering, and hence we expect that a water-cooled slotted crystal will perform even better than predicted here from this analysis.

Table 3: The bending magnet monochromator: Temperature and distortion results. PHF is the peak heat flux on the crystal surface, T_{max} is the maximum temperature on the crystal surface, T_{btf} is the maximum temperature at the bottom of the face plate, T_{max} is the maximum temperature rise above the coolant temperature (25°C). The total slope error is defined as a peak-to-peak value of the slope profile. The Si(111) Darwin width is given for comparison.

Energy [keV]	Bragg [deg.]	PHF [W/mm^2]	T_{max} [°C]	T_{btf} [°C]	T_{max} [°C]	Maximum Slope [μrad]	Darwin Width [μrad]
4	29.6	0.40	32.5	32.4	7.5	20.0	76
8	14.3	0.20	30.0	29.9	5.0	11.0	33.9
16	7.1	0.10	28.2	28.1	3.2	6.0	16.6
24	4.7	0.07	27.3	27.2	2.3	4.5	11.0
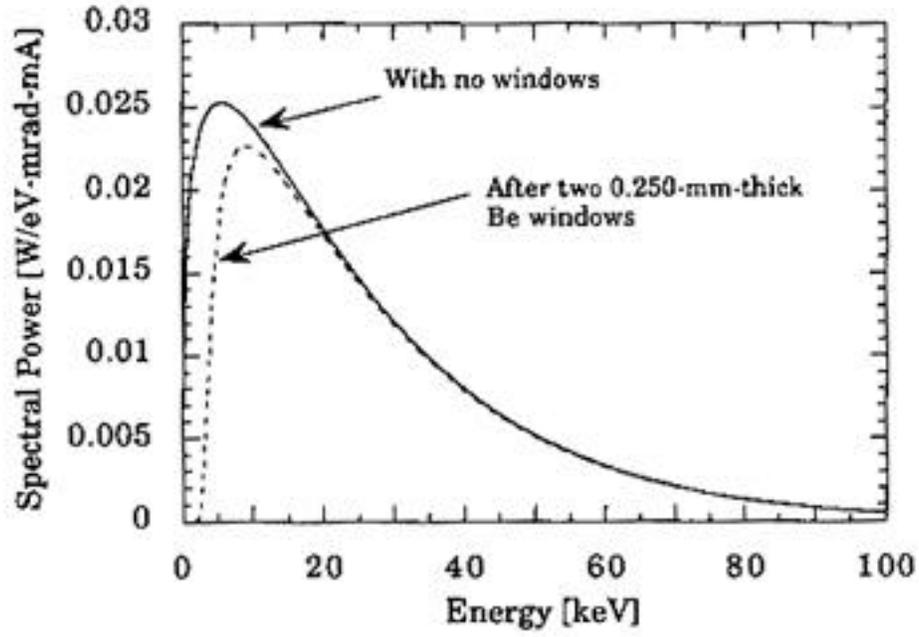
Fig. III.1: The APS bending magnet spectral power before and after two 0.250-mm-thick Be windows, at a ring energy of 7 GeV. The integration was done over the vertical angle only.
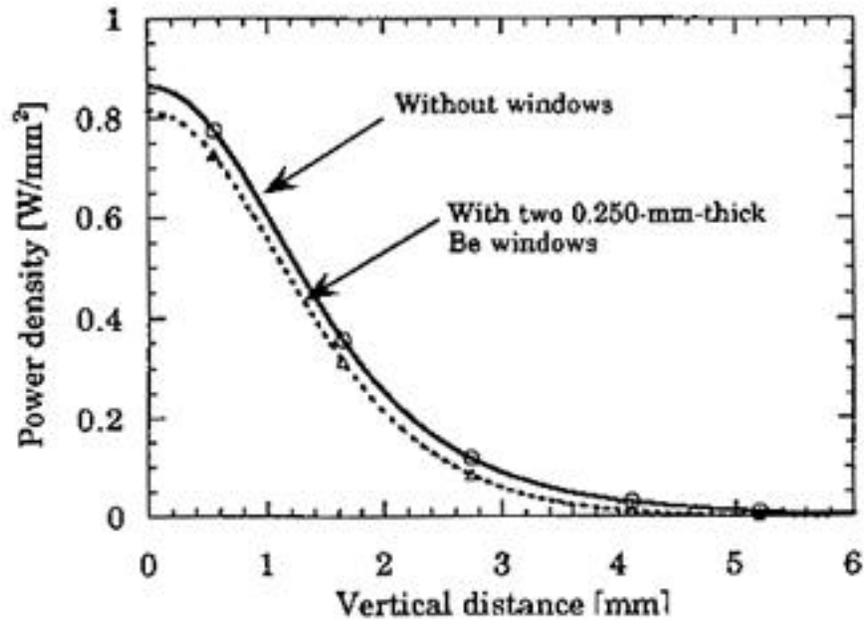
Fig. III.2: The APS bending magnet spatial power density profile in the vertical direction, at 30 m from the source, at normal incidence, for a ring energy of 7 GeV and a current of 100 mA.

Perspective view

X-ray Beam

Coolant

End view

1 mm   1 mm

5 mm   0.5 mm

30 mm

Y

X

The simulated channel-cell

Y

Z

X
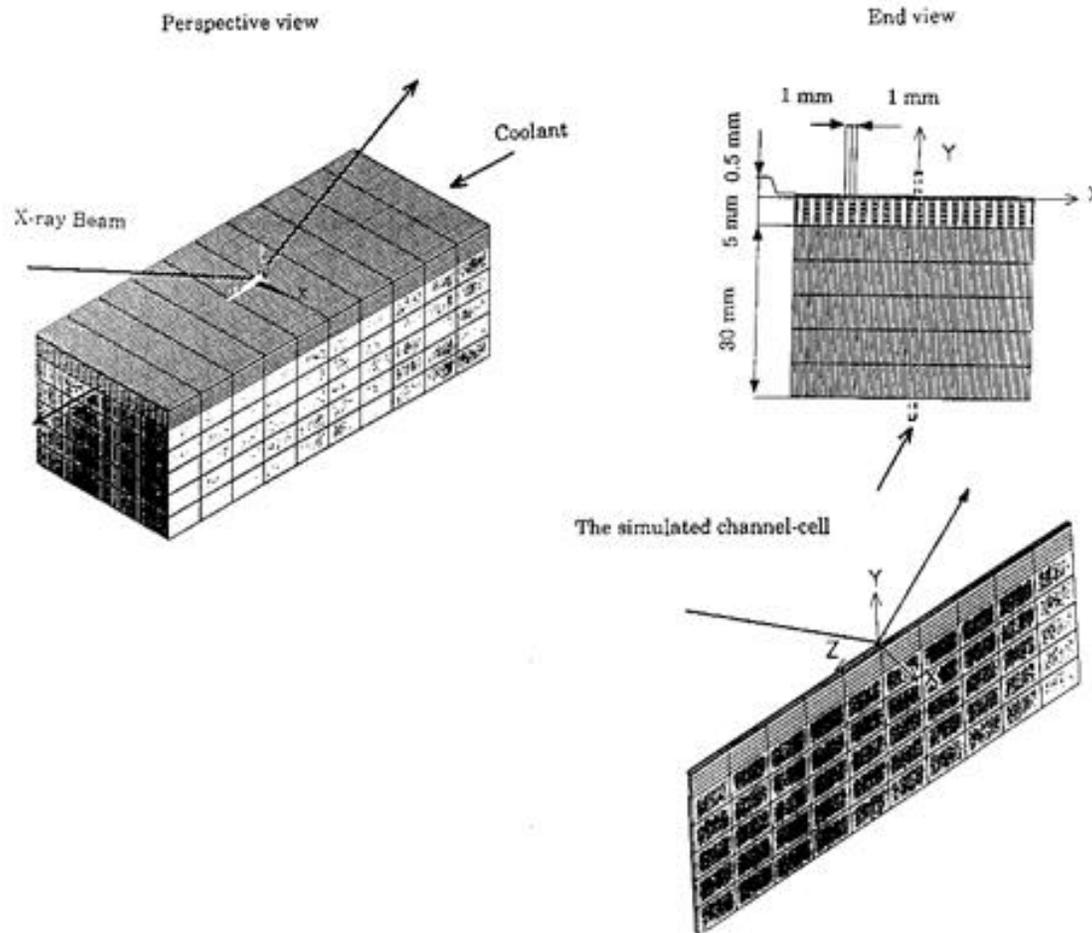
Fig. III.3: The crystal geometry chosen for the finite element analysis. For clarity, the exact number of channels and elements is not shown. Because the bending magnet beam power profile is uniform in the horizontal direction, only one channel-cell was used to model the crystal.
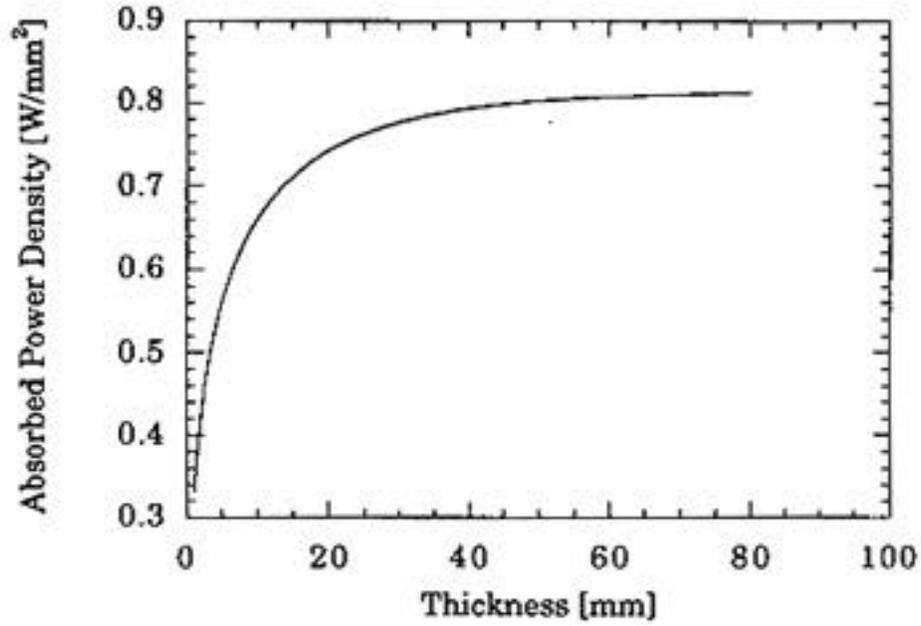
Fig. III.4: Absorbed power density, as a function of thickness, at 30 m from source, by a silicon crystal subjected to an APS bending magnet beam operating at 7 GeV and 100 mA. The calculation was performed by dividing the crystal into several layers and calculating the difference between the incident and the absorbed power density for each layer.
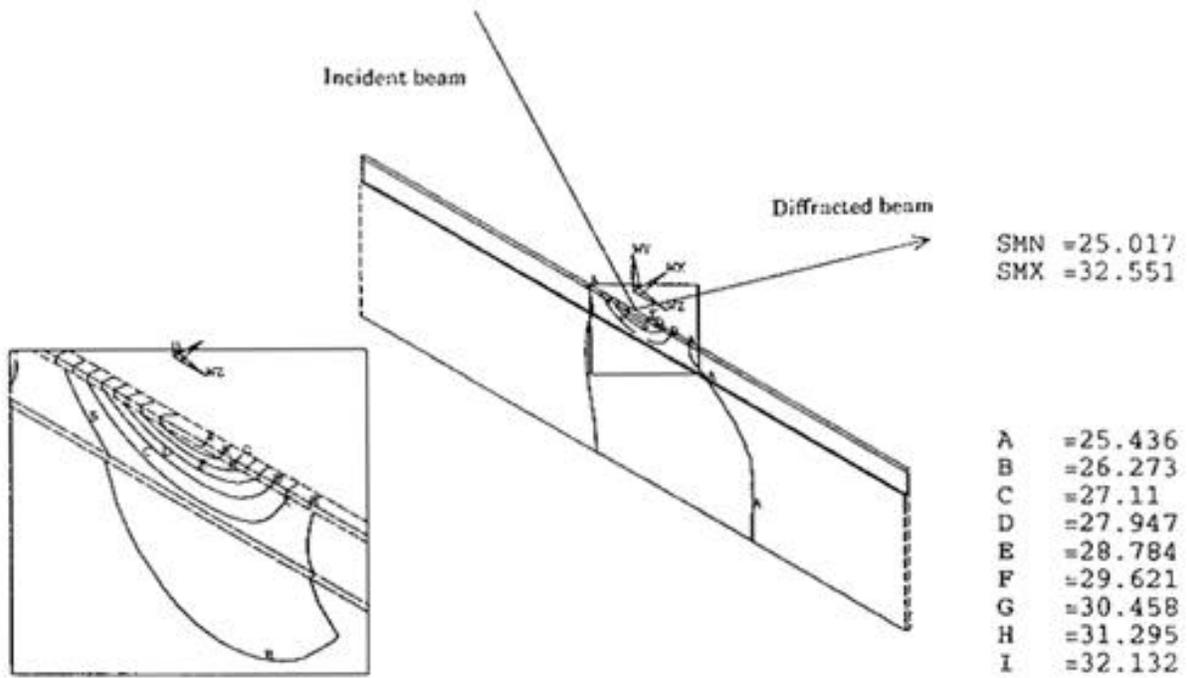
Fig. III.5: Temperature profile, in °C, within a Si(111) crystal oriented to diffract 4 keV photons. The plot shows the simulated channel-cell, which is located at the crystal center line, along the beam direction. For clarity, the coordinate system is offset in the y-direction. SMX and SMN are the maximum and minimum temperatures, respectively.
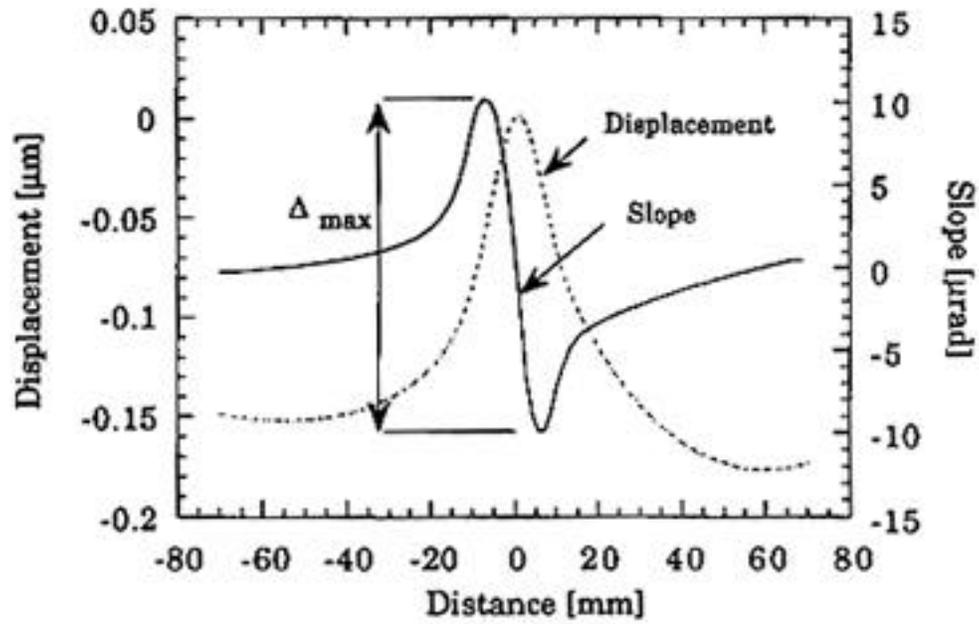
Fig. III.6: Displacement and tangential slope error profile along the center line of a Si(111) crystal oriented to diffract 4 keV photons from the APS bending magnet source at 30 m from the source. Calculations are for 7 GeV and 100 mA operation.
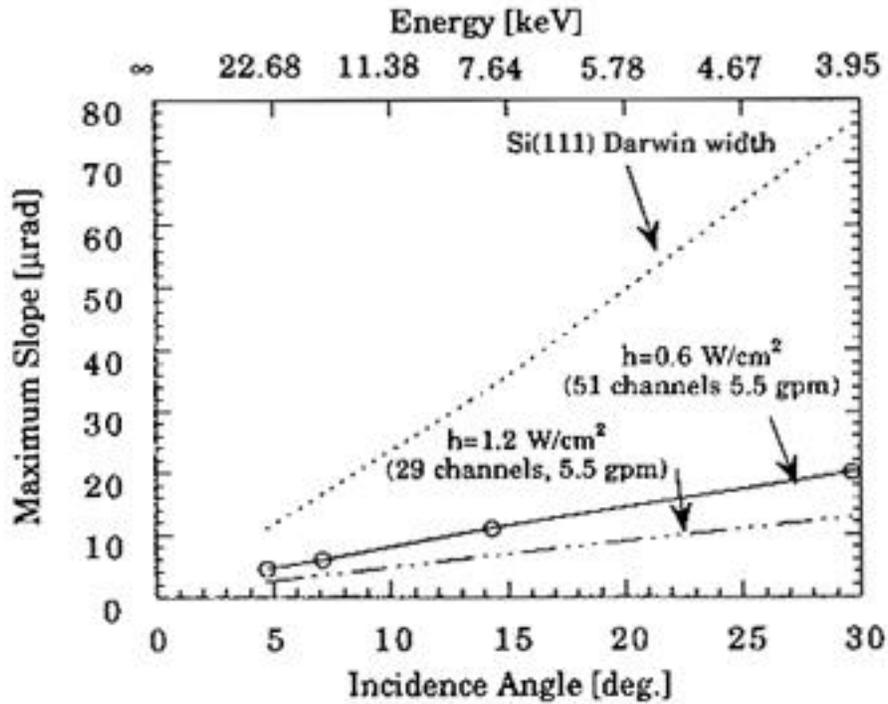
Fig. III.7: The bending magnet monochromator: Variation of the total thermally induced slope error as a function of Bragg's angle (bottom axis) and the corresponding energy (top axis) for a Si(111) crystal. The results are plotted for crystals with 51 and 29 channels with a fixed flow rate of 5.5 gpm of water. For comparison, the Si(111) Darwin width is also shown.

IV. The Wiggler A Monochromator

A. Properties of the source

1. Wiggler A parameters

The detailed characteristics of wiggler A can be found in reference 28; some of the important parameters for a gap of 2.1 cm are listed in Table 4.

Table 4. Wiggler A Parameters for a 2.1-cm Gap.

Parameter	Value
Wavelength, [cm]	8.5
Number of Periods, N	28
Device Length, L [m]	2.4
Magnetic Gap [cm]	2.1
Deflection Parameter, K	7.9
Maximum Field, B_{eff} [T]	1.0
Critical Energy, E_c [keV]	32.6
Total Power [kW]	7.4
Peak Power Density [kW/mrad^2]	73.0

2. Total power, heat flux, and source spectrum

The total power emitted by wiggler A with a 2.1-cm magnetic gap at a ring energy of 7 GeV and 100 mA current is about 7.4 kW. The standard APS front-end configuration for a wiggler beamline contains two 0.250-mm-thick beryllium windows at 25 m from the source. These beryllium windows are protected by two 0.300-mm-thick graphite filters located at 22 m from the source. Fig. IV.1 shows the source power spectrum for K=7.94. (Note that the graphite filters absorb most of the low-energy photons, particularly below 5 keV.) Fig. IV.2 shows the corresponding power density profile at 30 m from the source, the monochromator location. At this distance, the peak normal heat flux after the windows and filters is about 75 W/mm^2, and the beam size is about 29 mm (horizontal FWHM) by 2.7 mm (vertical FWHM).

B. Description and analyses of the crystal

1. Crystal geometry and cooling parameters

The geometry used for the finite element model is similar to that of the bending magnet crystal (see Fig. III.3), except that the height of the channels was reduced to 3 mm and liquid gallium is used as the coolant. A smaller channel height was chosen because of the better thermal conductivity of liquid gallium. Additionally, in order to reduce the pressure-induced deformation due to the liquid-gallium flow, the thickness of the crystal face plate was increase to 0.7 mm.

The coolant flow rate was chosen to be 4 gpm, flowing in 17 channels. This corresponds to a fluid velocity of about 4.95 m/s. The heat transfer coefficient, evaluated using Lyon's equation (Eq. 2), is about 21.8 W/cm^2-K. The average coolant temperature was set to 50°C.

Here also, one half channel was used to compute the maximum distortions on the crystal surface under the wiggler A beam. The goal of this study is to evaluate the maximum distortions of the crystal surface in the direction of the x-ray beam (tangential slope error). The maximum temperature gradient and, consequently, the maximum thermally induced slope error occur at the crystal midplane. Therefore, the channel located along the crystal center line was used for the finite element model. As mentioned in the bending magnet section, this approach saves considerable computation time and leads to only slightly conservative results (about 15% error in terms of thermally induced slope error) compared to those for the full crystal model. Note, however, that the performance of a monochromator is ultimately measured by its rocking curve. Experimentally, a rocking curve is obtained by recording the intensity of the diffracted beam from the second crystal of a double-crystal monochromator, by rocking its angle. Computationally, it can be obtained from the calculated distortion profile of the entire crystal, and therefore one needs to model one half of the crystal. This task will be performed in the near future.

2. Power load and boundary conditions

The power deposited in the crystal was computed following the same procedure as for the bending magnet case. The crystal was divided into several layers, and the power density profile absorbed by each layer along the beam optical path was calculated. Fig. IV.3 shows the variation of the absorbed power density as a function of thickness for a silicon crystal subjected to the wiggler A beam at a 2.1-cm gap. These calculations took into account the standard windows and filters. The total power deposited in these filters and windows is about 1370 watts (1296 watts for the filters and 74 watts for the windows). The total incident power at the monochromator is about 5.72 kW and the peak heat flux is about 75 W/mm^2.

Here, because a large amount of power is contained in the high-energy x-rays, assuming surface absorption of the entire incident beam is unrealistic. This is particularly true at large incidence angles (low x-ray energies) where the beam path length through the face plate is shorter. For the wiggler A beam at 2.1-cm magnetic gap, when surface absorption of the entire incident beam is assumed, the FEAs predict melting for a Si(111) crystal set to diffract 4-keV photons (Bragg's angle = 29.62°). For the chosen geometry, the face plate absorbs only about 40% of the incident

power. A large fraction of the transmitted x-ray beam through the face plate will fall in the channels and will be absorbed and transported by the liquid gallium (a relatively high-Z material). Calculations performed using PHOTON2 showed that, for the case of 4-keV reflection, only 6% of the incident peak power density remains after the beam traverses the coolant. Note, however, that our calculations are conservative in a sense that no attempt was made to consider the loss of power from Compton scattering.

All the analyses were performed assuming a wiggler A beam at 2.1-cm gap (K=7.94, E_c=32.6 keV). The power absorbed is treated as a heat generation rate in the thermal analysis. The absorbed power by the coolant was taken into account. The power distribution was used to evaluate the temperature distribution and the corresponding distortion field. The structural analysis boundary conditions are the same as for the bending magnet crystal (see Section III.B).

C. Temperature and distortion results

The performance of the crystal was studied as a function of Bragg angle. Table 5 summarizes the FEA results. Fig. IV.4 shows the temperature profile as the beam traverses the crystal. The crystal was set to diffract 8 keV photons from (111) planes (14.3° Bragg angle). As we can see from this figure, some heating occurs in the crystal base, along the beam path, and near the back surface. As a result, the crystal bows upward, compensating to some degree the distortions due to the power deposited on the crystal surface. This is evidence that one might design adaptive optics that use the heat load from synchrotron radiation itself. Fig. Iv.5 shows the variation of the effective thermally induced slope error as a function of the beam incidence angle at 2.1 cm magnetic gap. For comparison, the symmetric Si(111) Darwwin width and the corresponding energy are also plotted. For example, for a Si(111) crystal set to diffract 8 keV photons (Bragg angle of 14.3°), the total thermally induced slope error would be about 54 µrad, compared with the intrinsic Darwin width of about 34 µrad.

The FEA results plotted in Fig. IV.5 suggest that the use of slotted Si(111) crystals with gallium cooling and with a 2.1-cm-gap wiggler A will lead to severe thermal distortions for x-ray energies below 20 keV. At about 16 keV (7° incidence angle), the thermally induced slope error becomes comparable to the Darwin width, while at 24 keV, the slope error becomes larger than the Darwin width again. At low incidence angles (higher energies), although the surface power is lower, the total absorbed power is much higher due to the increased optical path as the beam traverses the crystal. These simulations clearly show that, for the APS wiggler A, additional methods for reducing the power load are required; some of the possible options are proposed below.

1. Asymmetrically cut crystal option

Fig. IV.5 indicates that, in order to minimize thermal slope errors, one should work at low incidence angles. Depending on the scanning range required, this can be done by using an asymmetrically cut crystal. However, note that the use of asymmetric crystals in a double-crystal monochromator also entails a greater sensitivity to thermal distortions. This, together with energy tunability range and an increased photon acceptance of thw asymmetric crystal are all issues that have to be weighed when considering the use of asymmetric crystals. An asymmetrically cut monochromator with adjustable asymmetry is currently under development at the APS [13]. This monochromator will allow one to increase the energy scanning range, and at the same time, to spread the beam footprint on the crystal surface [13].

2. Gap opening and filter options

Depending on the energy, possible way to reduce the power load are to open the wiggler gap or use filters or a combination of both. In this section, we describe various scenarios related to the gap opening and the use of filters. Fig. IV.6 shows the plot of the normal incidence peak heat flux at 30 m from the source as a function of the deflection parameter. Figs. Iv.7 and 8 show the brilliance and integrated flux as a function of energy for several gap sizes.

From Fig. IV.7, it can be seen that the peak brilliance of the wiggler beam is independent of the magnetic gap opening. Thus, if beam brilliance is the parameter of interest, the user should set the brilliance peak to the energy of interest. For energies below 32 keV, this will mean a gap size larger than 2.1 cm. In addition to increasing the brilliance, opening the wiggler gap also dramatically reduces the heat flux on the crystal. However, as shown in Fig. IV.8, opening the gap reduces the total incident photon flux.

As an example, we studied the case in which the user is interested in 10 keV photons. Table 6 summarizes the results of the various scenarios. By opening the wiggler gap so that the peak brilliance occurs at 10 keV (~ K=2.44), the gain in brilliance incident on the crystal over that of the 2.1 cm gap (K=7.94) is about 30%. In addition, the surface peak heat flux (assuming an incidence angle of 11.4°) on the crystal drops from 14.8 W/mm^2 to 3.6 W/mm^2. The total power impinging on the crystal also drops from 5.8 kW to about 0.35 kW (the absorption by the graphite filters and windows is taken into account). This will greatly reduce the thermal distortions on the crystal. Thus, by opening the wiggler gap, the brilliance of the 10 keV photons impinging on the crystal is increased, and, due to the smaller thermal distortions (compared to the case of K=7.94), the brilliance will be better preserved through the monochromator. However, as seen in Fig. IV.8, the total number of 10 keV photons produced by a K=2.44 wiggler is only about 25% that for the case where K=7.94. On the other hand, due to the severe heat flux for the case of K=7.94, the thermal distortions would certainly reduce the photon flux throughput. Thus, it may be that, realistically, the open gap situation may actually yield not only increased brilliance but increased total photon flux through the monochromator as well.

Now, let us assume that we are interested in maximizing the total number of 10 keV photons through the monochromator. Additionally, we assume that we can tolerate total slope errors on the crystal of about half of the intrinsic Si(111) Darwin width for that energy. Based on the results of the FEA studies, we compared the total flux incident on the crystal from opening the gap and leaving the gap closed (2.1 cm), but using filters to reduce the heat load. Fig. IV.9 show the results of calculations using PHOTON2 simulating the flux at a 2.1 cm gap (K=7.94) with and without various filters and the flux at opened gap with K=3.88. The flux and power densities are given after the standard 0.600 mm of graphite filters and 0.500 mm of Be windows, at 30 m from the source. The gap opening and the filters were chosen so that, with the crystal at an incidence angle of 11.4° (10 keV, Si(111)), the surface power density on the crystal would be about 6.4 W/mm2. This surface power density was chosen based on the FEA studies (Fig. IV.5), and it corresponds to a thermal distortion of about 14 μrad on the crystal (about 52% of the Darwin width). Note that the actual thermal distortions should be less because the FEA studies were based on the case where K=7.94 and the total power was about 7.4 kW; whereas the total power after the filters or a more open wiggler gap will be considerably less. The flux for the closed gap (K=7.94) without filters is shown for comparison. Fig. IV.9 shows that, if one is interested in working at 10 keV with Si(111) and can tolerate a 14 μrad total thermal distortion, it is much better to open the gap of the wiggler than to use filters with a closed gap. The filters would absorb all the desired 10 keV photons. In this case, the flux (for 10 keV photons) incident on the crystal at K=3.88 is about 40% of that at K=7.94 with no filter.

However, if the user is interested in higher energies (> 25 keV), the use of filters may be a better option for maximum flux. Note that the above only compares the flux incident on the crystal and not the actual flux after the crystal. To predict the actual flux after the crystal would require a detailed ray-tracing simulation, possibly using SHADOW [29], that incorporates the thermal distortions of the crystals. Clearly, a case-by-case study to optimize brilliance and/or flux is necessary.

Other alternative approaches include the use of a mirror as the first optical component [30], or cryogenically cooled thin crystals. Mirrors operate at much smaller incidence angles than Bragg reflections, therefore the heat fluxes are less severe. They can be used to cut off higher energy photons, thereby reducing the power load on the monochromator. Thin crystals have the advantage of absorbing less power and, when cooled with liquid nitrogen, may offer a solution. We are currently investigating this.

D. Conclusion

We have performed simulations for a liquid-gallium-cooled, slotted Si(111) crystal subjected to the wiggler A radiation in the worst-case scenario: a 2.1 cm magnetic gap, K=7.94 with critical energy at 32.6 keV (for 7 GeV - 100 mA operation). The FEA results clearly show that the use of Si(111) crystals with the chosen cooling scheme for the classical energy region of 4-20 keV will result in severe thermal distortions. Depending on the beam parameter of interest, energy, brilliance or total flux, and on the amount of distortion that is tolerable in the crystal, we have proposed various options. In the low-energy range, the best option to reduce the heat load is to

open the wiggler A gap. As an example, setting the wiggler at a gap of 4.75 cm (K=2.44) will reduce the peak heat flux on the crystal surface to the point at which it can be handled by a slotted crystal with liquid gallium cooling. The FEA calculations indicate that, in this case, the maximum slope error for a crystal set to diffract 10 keV photons (Bragg angle = 11.4°) is about 12.5 µrad (see Table 6) compared to the Darwin width of 27 µrad for the Si(111) reflection. For this particular wiggler A gap value of 4.75 cm, the brilliance of the 10 keV photons is optimized at the expense of the incident flux on the crystal. However, depending on the amount of distortion that is tolerable, by setting the wiggler gap to a lower value (higher K), one may optimize the total number of 10 keV photons through the crystal. Detailed ray-tracing simulations will be required to predict the optimum K value that would yield a maximum photon throughput. Either way, opening the wiggler gap significantly reduces the heat load on the crystal. In the high-energy range (> 25 keV), the use of filters may be more appropriate. Here, opening the gap (from 2.1 cm) will reduce both the brilliance and the total flux incident on the crystal.

Other approaches to reduce the heat load on the crystal include the use of mirrors as power filters [30], cryogenically cooled thin crystals, and asymmetrically cut crystals with adjustable asymmetry [13].

Table 5: Wiggler A crystal: Temperature and structural results. PHF is the peak heat flux on the crystal surface, T_{max} is the maximum temperature on the crystal surface, T_{max} is the maximum temperature rise above the coolant temperature (50°C). The Si(111) Darwin width is given for comparison.

Energy [keV]	Bragg [deg.]	PHF [W/mm^2]	T_{max} [°C]	T_{max} [°C]	Maximum Slope [µrad]	Darwin Width [µrad]
8	14.3	18.5	108.0	58.0	54.0	33.9
16	7.1	9.27	88.0	38.0	18.0	16.6
24	4.7	6.14	80.0	30.0	14.0	11.0
56.65	2.0	2.61	65.8	15.8	12.0	4.7

Table 6: Summary of scenarios for 10 keV photons. E is the photon energy, K is the deflection parameter, Ec is the critical energy, Pd is the peak heat flux on the crystal surface. The Darwin width is for Si(111) reflection. Note that all calculations include the 0.600-mm-thick graphite filters and the 0.500-mm-thick Be windows before the monochromator location, and that maximum slope errors are based on the results of the FEA for the 2.1-cm-gap case.

E [keV]	Scenario	Gap size [cm]	K	Ec [keV]	Fraction of the incident 10 keV photons	Incident power [kW]	Pd [W/mm²]	Maximum slope [μrad]	Darwin width [μrad]
10	Gap opening	4.75	2.44	10.0	25%	0.35	3.6	12.5	27
		3.65	3.88	15.9	40%	1.1	6.4	14.0	
	Filters: 18 mm C	2.1	7.94	32.6	0.011%	2.0	6.4	14.0	
	No filters	2.1	7.94	32.6	100%	5.8	14.8	38.0	
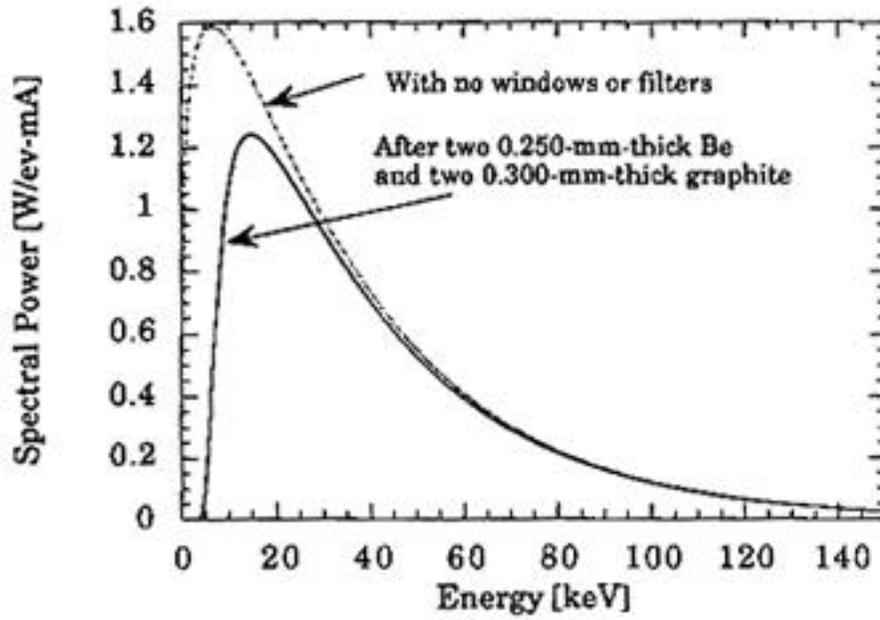
Fig. IV.1: Wiggler A [= 8.5 cm] spectral power with and without beryllium windows and graphite filters. The plots are for a 2.1 cm magnetic gap case, a ring energy of 7 GeV, and a current of 100 mA.

(a)

(b)
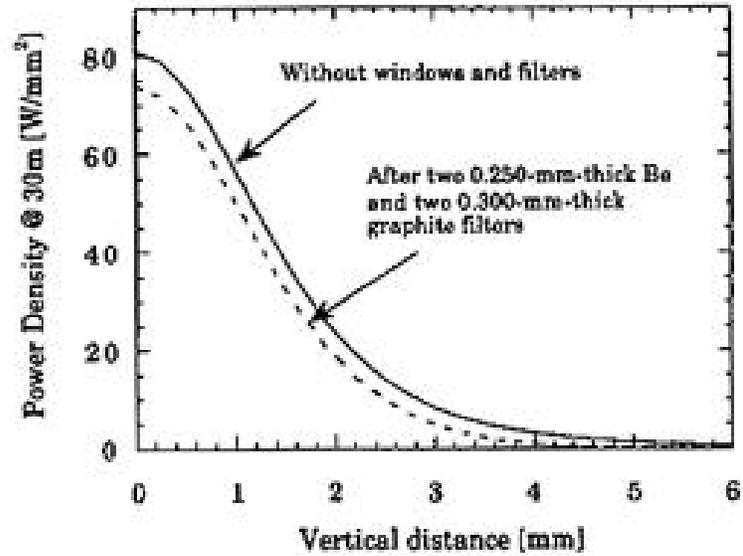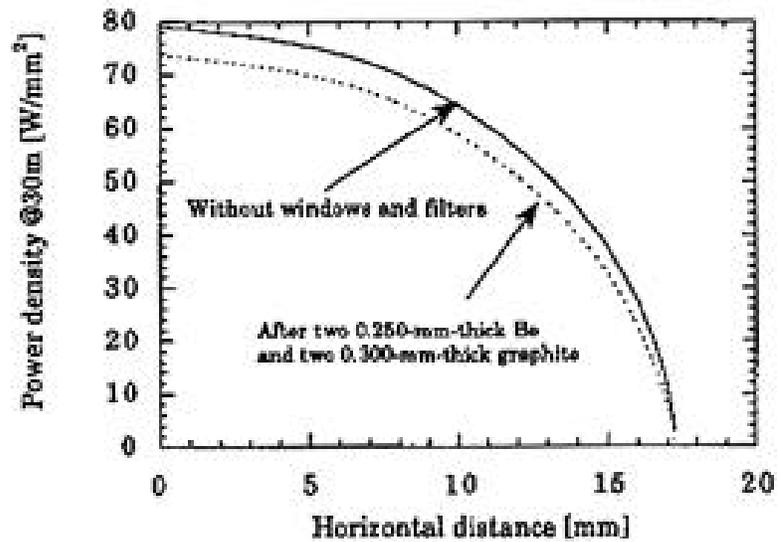
Fig. IV.2: Wiggler A [λ = 8.5 cm] (a) vertical and (b) horizontal spatial power density profiles at 30 m from the source, for 7 GeV - 100 mA operation.
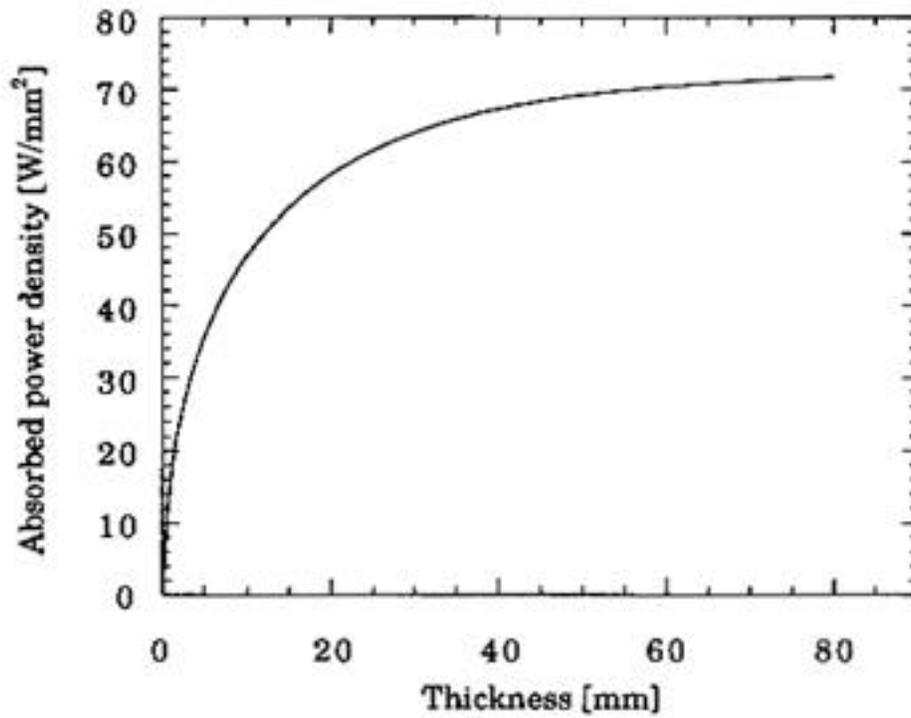
Fig. IV.3: Absorbed power density, as a function of thickness, at 30 m from the source, by a silicon crystal subjected to APS wiggler A (2.1 cm gap, K = 7.94) operating at 7 GeV and 100 mA. The calculation was performed by dividing the crystal into several layers and calculating the difference between the incident and the absorbed power density for each layer.

A	=53.344
B	=60.032
C	=66.72
D	=73.408
E	=80.096
F	=86.784
G	=93.472
H	=100.16
I	=106.848
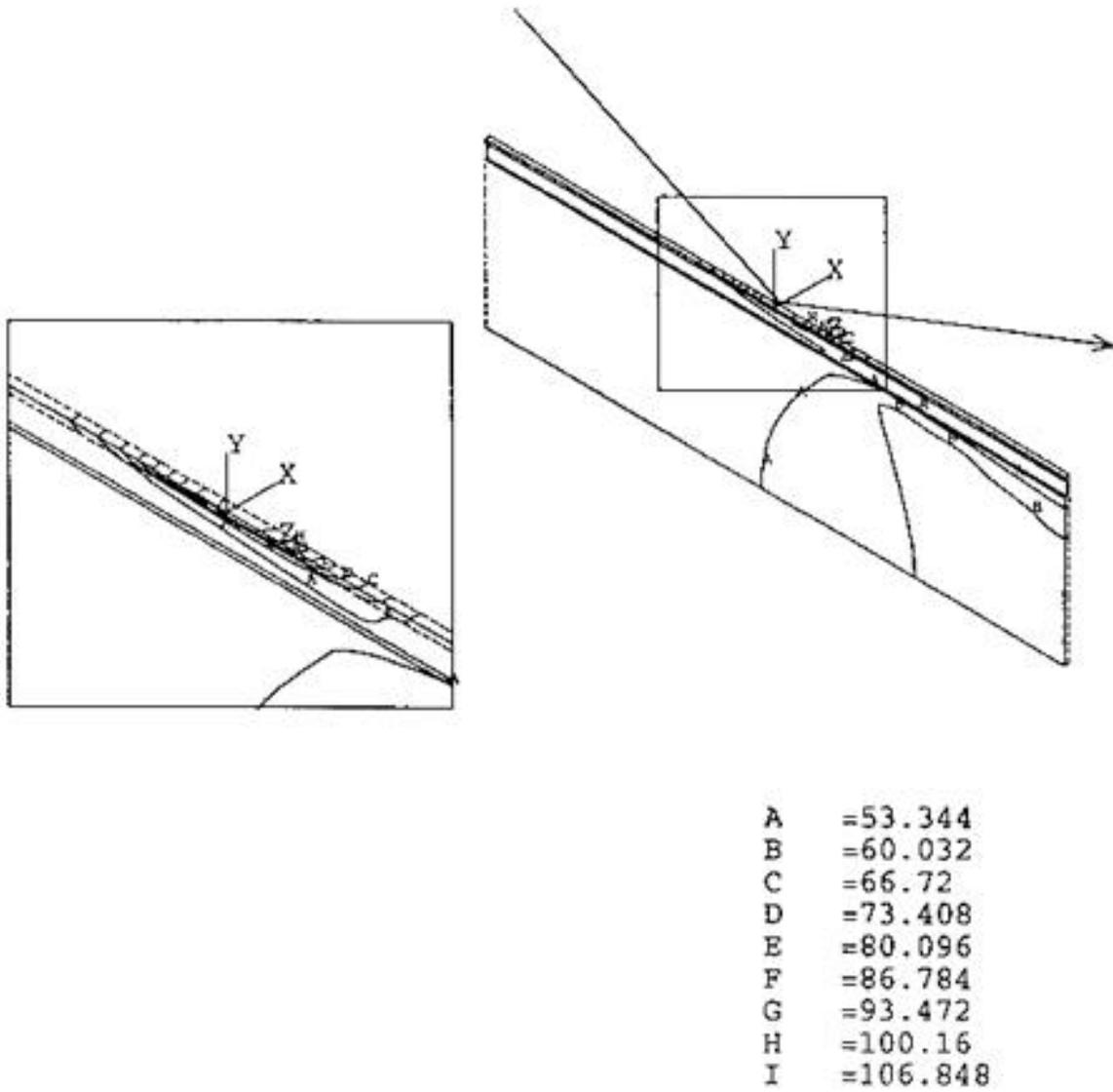
Fig. IV.4: Temperature profile, in °C, within a Si(111) crystal oriented to diffract 8 keV photons. The plots show the simulated channel cell, which is located at the crystal center line, along the beam direction.
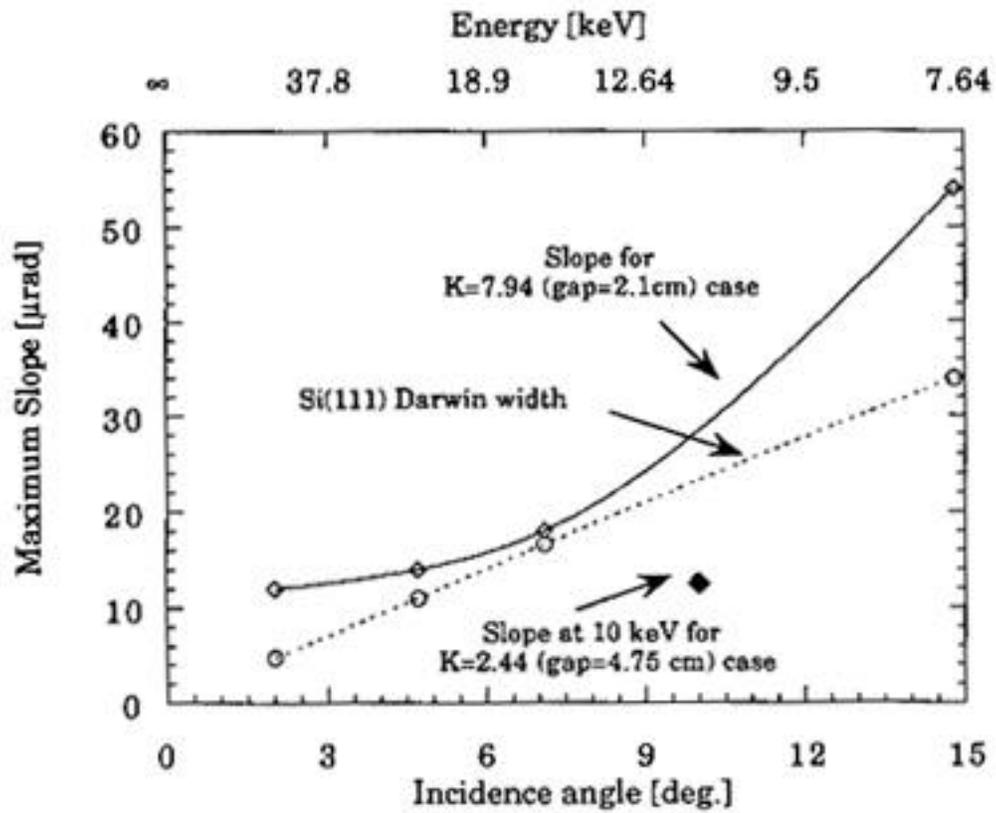
Fig. IV.5: Calculated total distortion as a function of incidence angle. For reference, the corresponding energy (top axis) and the Darwin width are also plotted for the Si(111) reflection.
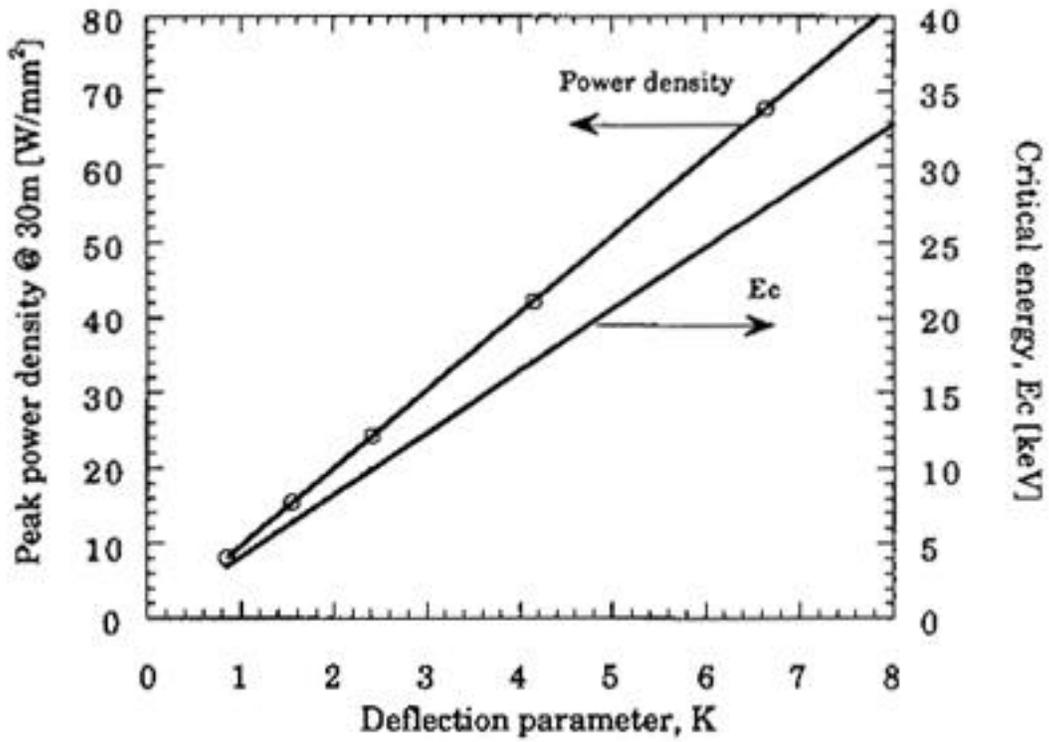
Fig. IV.6: Peak heat flux at 30 m from the source and the critical energy of wiggler A [= 8.5 cm] as a function of the deflection parameter for 7 GeV - 100 mA operation (data taken from ref. 28).
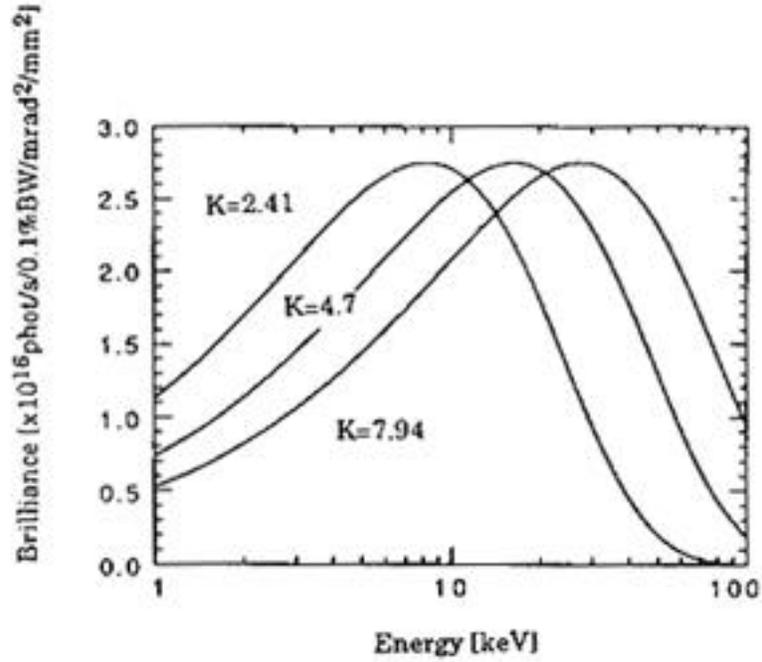
Fig. IV.7: On-axis brilliance spectra (plotted in log-log scale) for wiggler A operating at different gap openings [from ref. 28]. The plots are for 7 GeV - 100 mA operation.
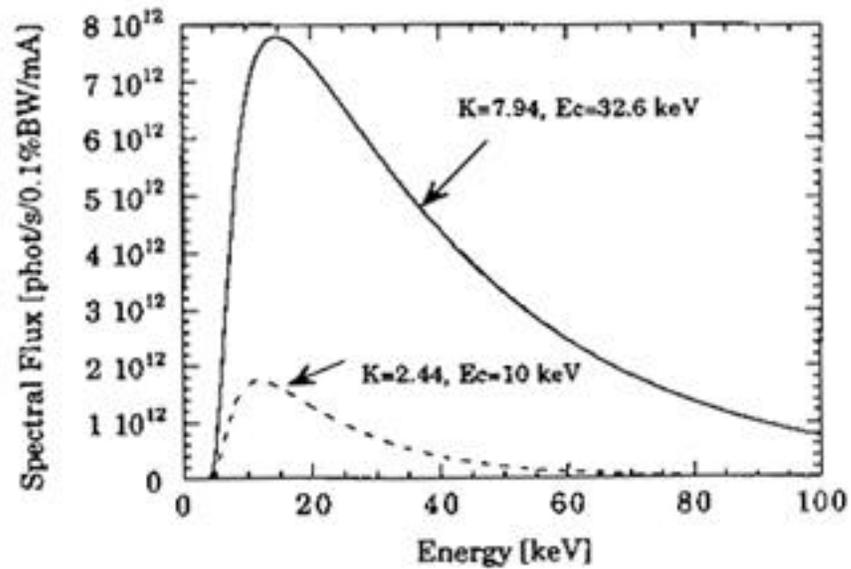
Fig. IV.8: Flux spectra for wiggler A operating at K = 2.44 (Ec = 10 keV), and K = 7.94 (closed gap). The plots are for 7 GeV - 100 mA operation.

30
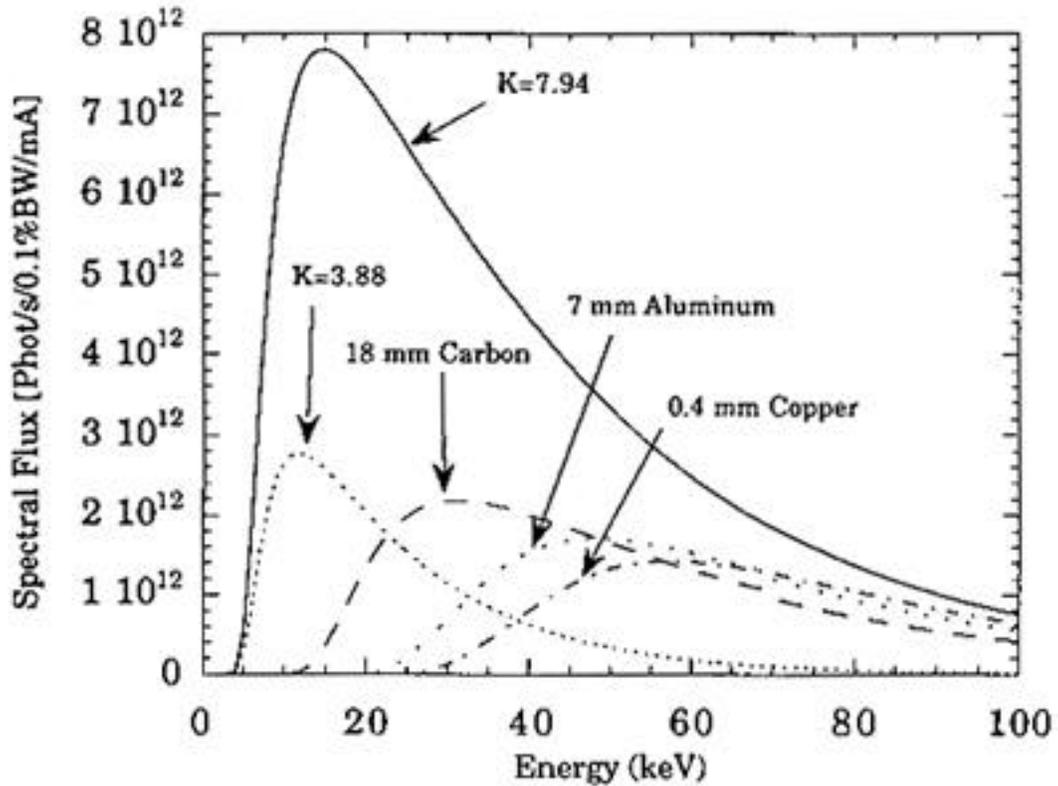
Fig. IV.9: Comparison of flux incident on the crystal between the case of a magnetic gap of 2.1 cm (K = 7.94, Ec = 32.6 keV) with a variety of filters and the case of 3.7 cm magnetic gap (K = 3.88, Ec = 15.95) with no filters. Flux calculations were performed with PHOTON2. This comparison is for a Si(111) crystal set to an 11.4° Bragg angle (10 keV). The filters and gap opening are set so that, based on FEA results, the total distortion on the crystal surface in half of the Darwin width of the reflection. The advantage of opening the wiggler A gap is clear in this case. At 3.7 cm gap (K = 3.88), the number of 10 keV photons is about 40% that produced by the wiggler at 2.1 cm gap (K = 7.94).

V. The Inclined Crystal for Undulator A

A. Properties of the source

1. Undulator A parameters

The APS undulator A parameters are listed in Table 7 [31].

Table 7: Undulator A Parameters

Parameter	Value
Undulator Period, [cm]	3.3
Number of Periods, N	72
Device Length, L [m]	2.4
Gap [mm]	12.87
Deflection Parameter, K_{eff}, (K_{max})	2.17 (2.19)
Magnetic Field, B_{eff} [T], (B_{max})	0.704 (0.7104)*
First Harmonic Energy, E_1 [keV]	4.2
Characteristic Energy, Ec [keV]	23.5
Peak Power Density [kW/mrad^2]	135
Total Power [kW]	3.8

* Measured Value

2. Power, heat flux, and source spectra

Simulations were performed for two different deflection parameters: K=2.17, corresponding to the first harmonic at 4.2 keV, and K=1.23, corresponding to the first harmonic at 8 keV.

At a ring energy of 7 GeV and a current of 100 mA, the total power and the normal peak heat flux (including beam emittance effects) generated by undulator A at 30 m from the source are:

For the first harmonic at 4.2 keV:
    Total power = 3.8 kW
    Peak heat flux = 140 W/mm^2
For the first harmonic at 8 keV:
    Total power = 1.18 kW
    Peak heat flux = 75 W/mm^2

Because it may be necessary to operate the undulator beamline in a windowless mode, no filters or Be windows were included in this worst-case calculation. The vertical and horizontal spatial power density profiles, calculated using the URGENT code [32], are given in Fig. V.1. The undulator A spectral power, calculated using the same computer code, is shown in Fig. V.2.

B. Description and analyses of the crystal

1. Crystal geometry and cooling parameters

For the inclined crystal (see Fig. V.3), the planes of diffraction make an angle   with the crystal surface, thereby spreading the power density on the crystal surface by a factor of 1/(sin   cos), where   is Bragg's angle. In the APS design [6], the inclination angle and energy range were originally chosen so that the power density on the crystal surface does not exceed about 5 W/mm^2 and the crystal is under 250 mm long [6]. The surface power density limit was chosen based on previous experimental and computer simulation results. The APS design calls for one set of Si(111) crystals with 85° inclination to cover the energy range from 4 to 9 keV, and for another set with 78° inclination to cover the 8 to 20 keV energy range. For further details on the concept and geometry of the inclined crystal refer to references 6-12.

Fig. V.4 depicts the geometry used for the FEA model. The crystal is cooled by flowing liquid gallium through rectangular channels. Similar to the wiggler A crystal, the channels are 1 mm wide and 3 mm deep; the thickness of the fins is equal to1 mm, and that of the crystal face plate is 0,7 mm. The channels are oriented transverse to the crystal (see Fig. V.4).

The coolant flow rate was chosen to be 4 gpm, flowing in 50 channels, which corresponds to a fluid velocity of 1.68 m/s. The heat transfer coefficient, estimated using equations (1) and (2), is about 18 W/cm^2-K. The coolant average temperature is set to 50°C, and its temperature rise is estimated to be 6°C.

2. Power load and boundary conditions

Because of the high inclination angles with which we are dealing, the crystal intercepts the beam at a very shallow glancing angle. Therefore we assume that the incident power is totally deposited on the crystal surface. The power density profiles calculated using the URGENT code are shown in Fig. V.1. To keep the sizes of the crystals reasonable, it has been assumed that slits could be used to let through only the central radiation cone. The slit opening at 30 m from the source is 3.6 mm in the horizontal direction and 1.8 mm in the vertical direction, which corresponds to > 4   of the central harmonic radiation cone. The total incident power is reduced to about 740 watts for K=2.17 (the first harmonic at 4.2 keV), and to about 400 watts for K=1.23 (the first harmonic at 8 keV). There has been concern, however, that the use of vertical slits introduces a sharp thermal gradient, thereby increasing the thermally induced slope, and this is also a question we sought to answer.

Here, the planes of diffraction are not parallel to the surface, and the overall structure is not symmetric. Therefore, the full crystal was modeled. The incident power is treated as absorbed on the surface in the finite element thermal analysis. The thermal distortions are calculated assuming that the crystal is fixed at the bottom face. This is a reasonable assumption with the crystal base is made relatively thick (several cm).

C. Temperature and distortion results

As mentioned previously, simulations were performed for two different deflection parameters: K=2.17 and 1.23. For K=2.17, the inclination angle, , is 85°, and for K=1.23, it is 78°. For each case, calculations were performed with and without vertical slits, and in all cases the horizontal slit opening is kept at 3.6 mm. The results of the analyses are summarized in Table 8. Fig. V.5 shows the temperature profile on the surface of a 78°-inclined crystal set to diffract 8 keV photons. The horizontal slit opening is set to 3.6 mm, while the vertical slits are left wide open. Figs. V.6 and 7 show the variation of displacement and the slope in the direction of the reciprocal lattice vector for the two cases. A comparison is made between the case where vertical slits are used and the case with no vertical slits.

Figs. V.6 and 7 reveal that, for an inclined geometry, the thermally induced slope error under the beam footprint has a constant sign. The peak slope error for the 4.2 keV case (and with 1.8 mm vertical slits), for example, is about 34 µrad. The peak slope error represents the maximum deviation from Bragg's angle. The effective thermally induced slope error, which contributes to the broadening of the rocking curve, is the difference between the peak slope and the slope at the edge of the beam. Its value for the 4.2 keV case with 1.8 mm vertical slits is about 21 µrad. This is to be compared with the Darwin width of 71 µrad.

For the 78°-inclined Si(111) crystal set to diffract 8 keV photons, the maximum effective slope error is only about 7 µrad (for 1.8 mm vertical slits). This is to be compared with the Darwin width of 33.9 µrad.

Regarding the effect of vertical slits, the FEA results indicate that the thermally induced slope error increases when a 1.8 mm vertical slit opening is used. The effect is worse for the 4.2 keV case, in which the use of slits almost doubles the effective slope error. Thus, vertical slits should be left open to minimize the slope errors. This can be done without affecting the crystal size because the length of the crystal depends mostly on the inclination angle and the horizontal size of the beam.

D. Conclusion

The above simulations predict that a gallium-cooled inclined crystal will perform reasonably well when subjected to the APS undulator A beam. For the worst-case scenario, 4.2 keV photons, 85° inclination angle, the effective thermal distortion (for the slitted beam) is only 21 µrad. This is to be compared with the Darwin width of 71 µrad for this reflection. For the case of

8 keV photons with 78° inclination, the effective thermally induced slope error for the slitted-beam case is about 7 μrad or 20% of the intrinsic Darwin width.

Overall, the results are encouraging. Even for the worst case studied (4.2 keV), the slope error is only about 30% of the Darwin width. For the 8 keV case presented above, further improvement is certainly possible by going to inclination angles higher than 78°. We chose 78° because we wanted to keep the surface power densities to less than about 5 W/mm2 and to have the crystal operate within the 8 to 20 keV range without the crystal size exceeding 250 mm. It is up to the individual crystal designers to balance allowable distortions, energy ranges, inclination angles, and crystal sizes to their needs. In general, we do not recommend inclination angles greater than 85° due to the difficulty in alignment.

Table 8: Temperature and distortion in the direction of the reciprocal lattice vector of an inclined Si(111) crystal subjected to an APS undulator A beam at 7 GeV - 100 mA operation. E_1 is the energy of the first harmonic,   is the inclination angle, PHF is the peak heat flux on the crystal surface, T_{max} is the maximum temperature on the crystal surface, T_{bfp} is the temperature at the bottom of the face plate, T_{fp} is the temperature drop across the crystal face plate, U_{max} is the maximum displacement. The slit opening is 3.6 mm X 1.8 mm at 30 m.

E_1 [keV]	(incl. angle)	Bragg	PHF [W/mm²]	Vertical slits config.	T_{max} [°C]	T_{bfp} [°C]	T_{fp} [°C]	U_{max} [μm]	Peak slope$_{max}$ [μrad]	Effective slope* [μrad]	Darwin width [μrad]
4.2	85°	28.06°	5.7	no slits	103.4	71.8	31.6	0.095	33.2	11.0	71.0
				with slits	93.2	66.4	26.8	0.064	33.8	21.0	
8	78°	14.30°	3.8	no slits	84.8	64.5	20.3	0.073	12.2	5.0	33.9
				with slits	78.3	61.0	17.3	0.052	13.2	7.0	

* The effective slope error is calculated for the central radiation cone and is defined as the difference between the peak slope and the slope at the edge of the beam.

(a)

(b)
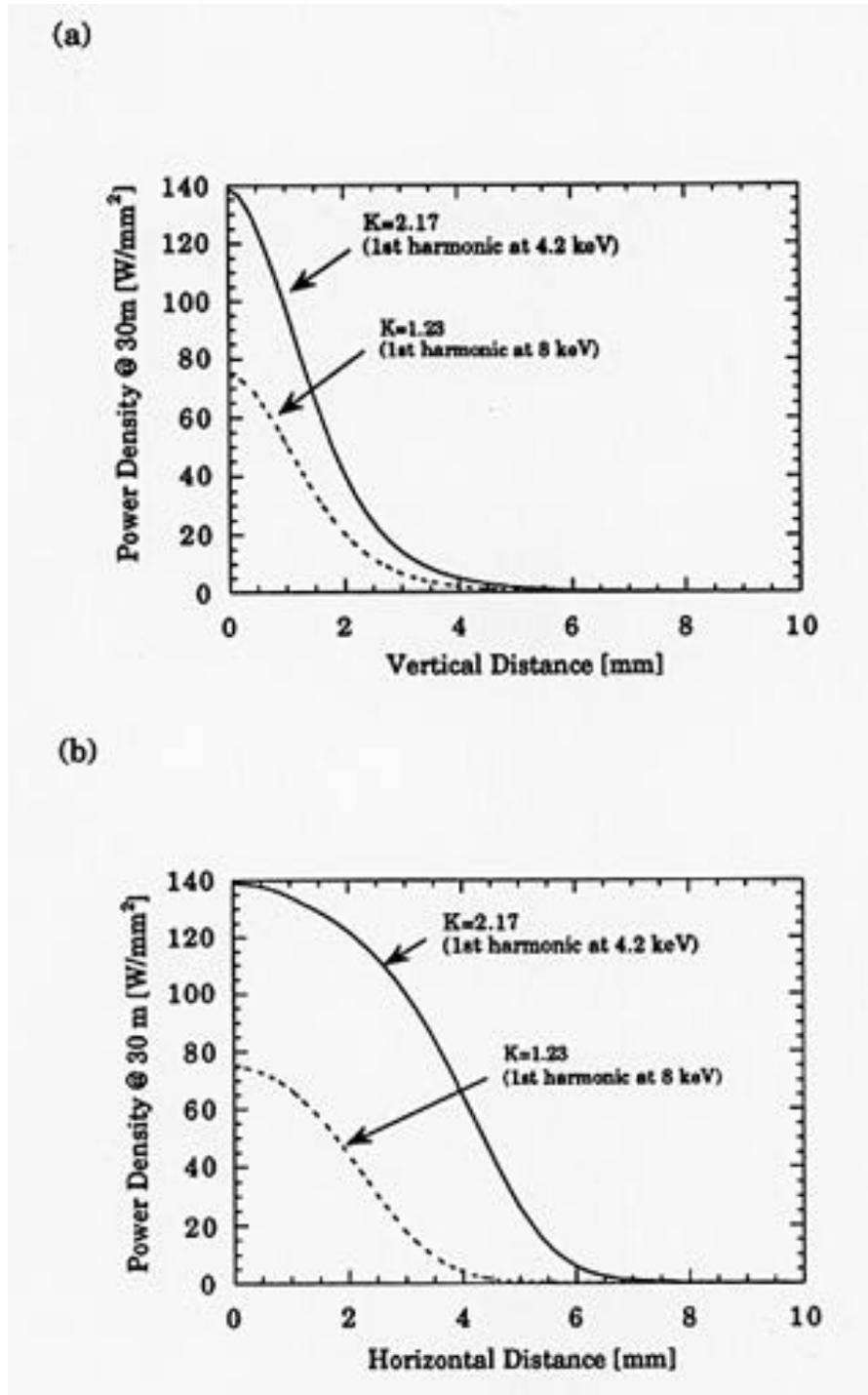
Fig. V.1: The APS undulator A (a) vertical and (b) horizontal power density profiles at 30 m from the source for K = 2.17 and 1.23. The profiles are for undulator A beam at a ring energy of 7 GeV and a current of 100 mA.
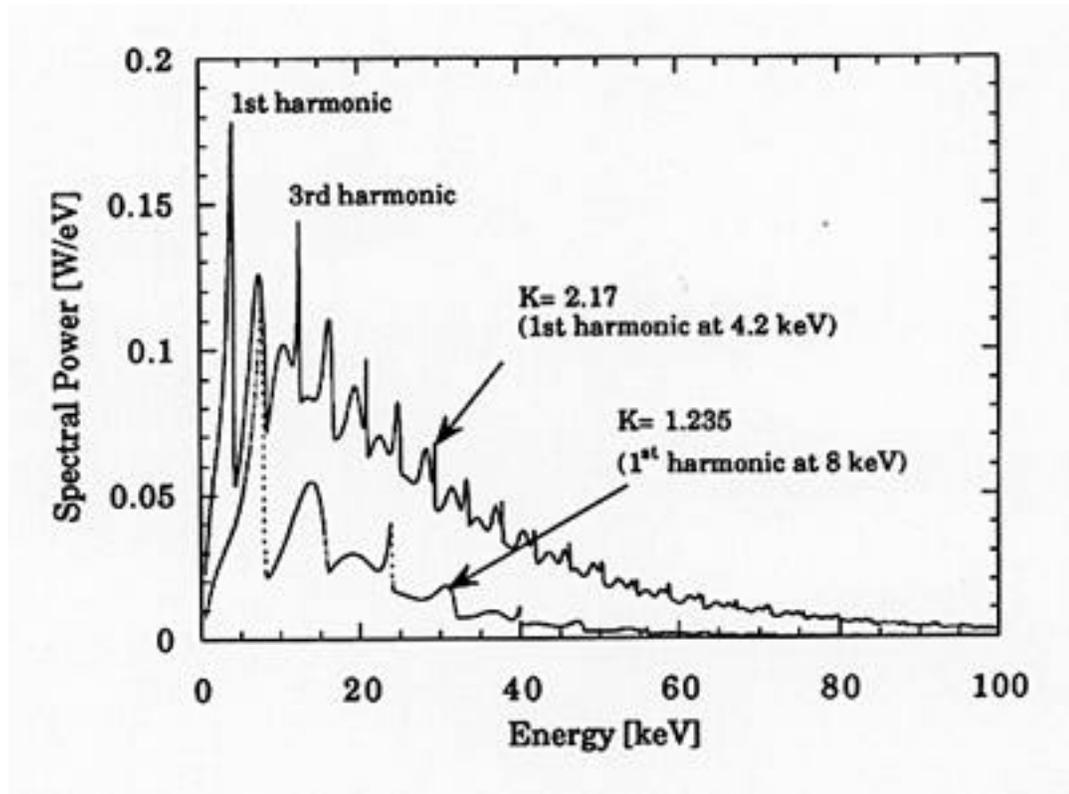
Fig. V.2: The APS undulator A power spectra for K = 1.235 (E = 8 keV) and for K = 2.17 (E = 4.2 keV). The plots are for a ring energy of 7 GeV and a current of 100 mA. The total powers are 1.18 kW for K = 1.235 and 3.65 kW for K = 2.17.
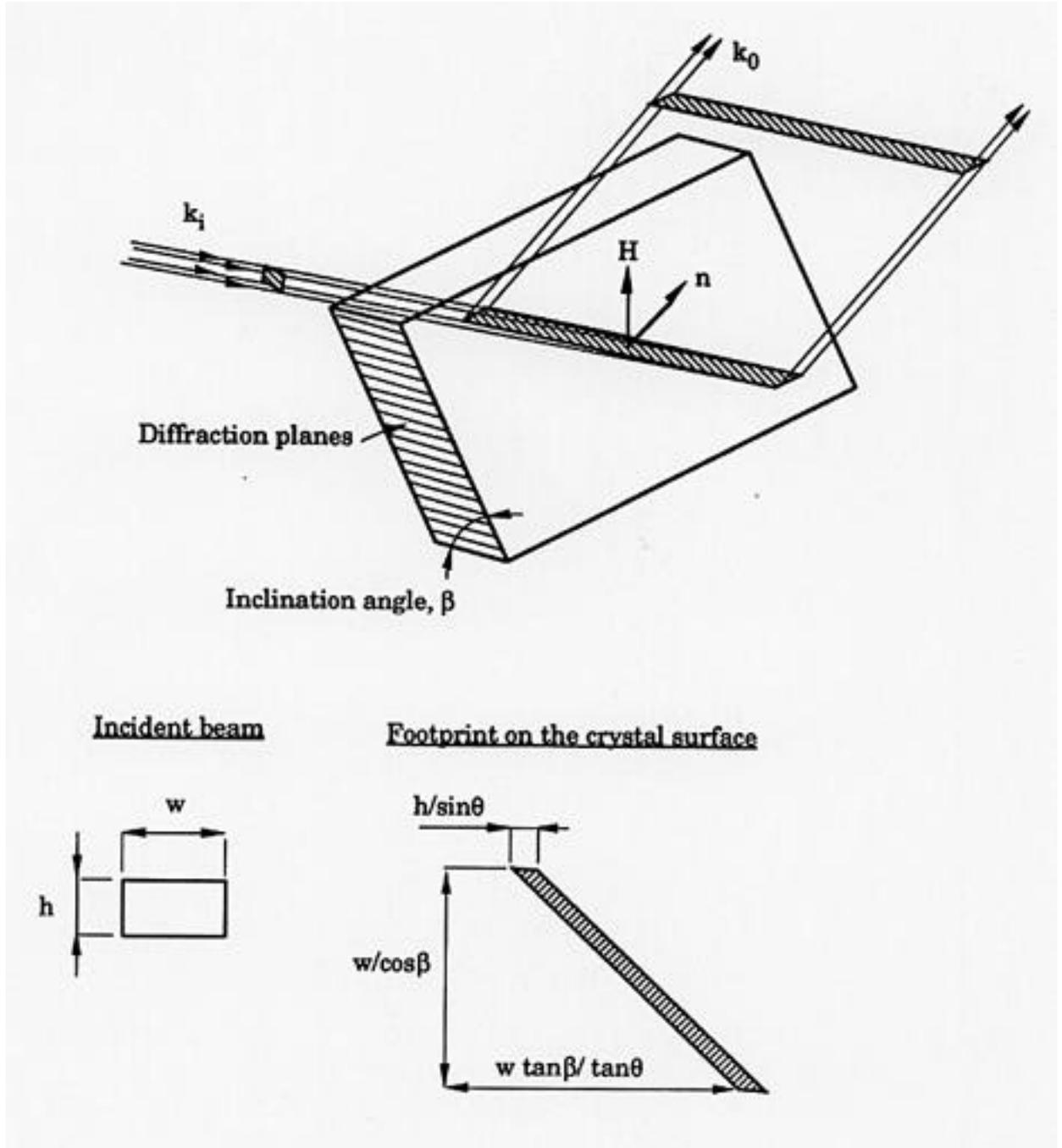
Fig. V.3: The inclined crystal geometry
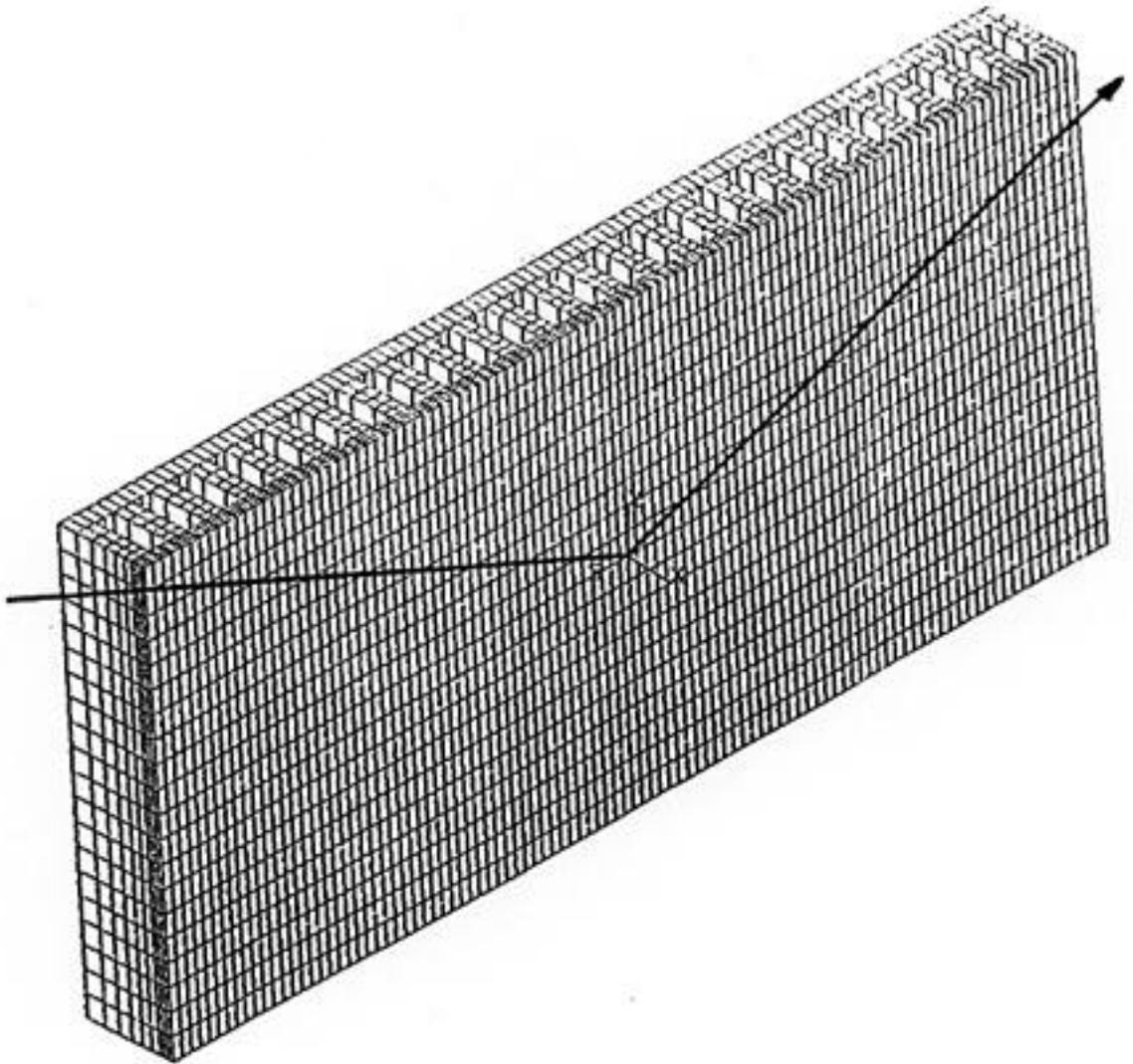
Fig. V.4: The geometry chosen to model the inclined crystal. In this case the channels are oriented along the width of the crystal. They are 1 mm wide and 3 mm deep. The thickness of the fins is 1 mm each and that of the face plate is 0.7 mm.
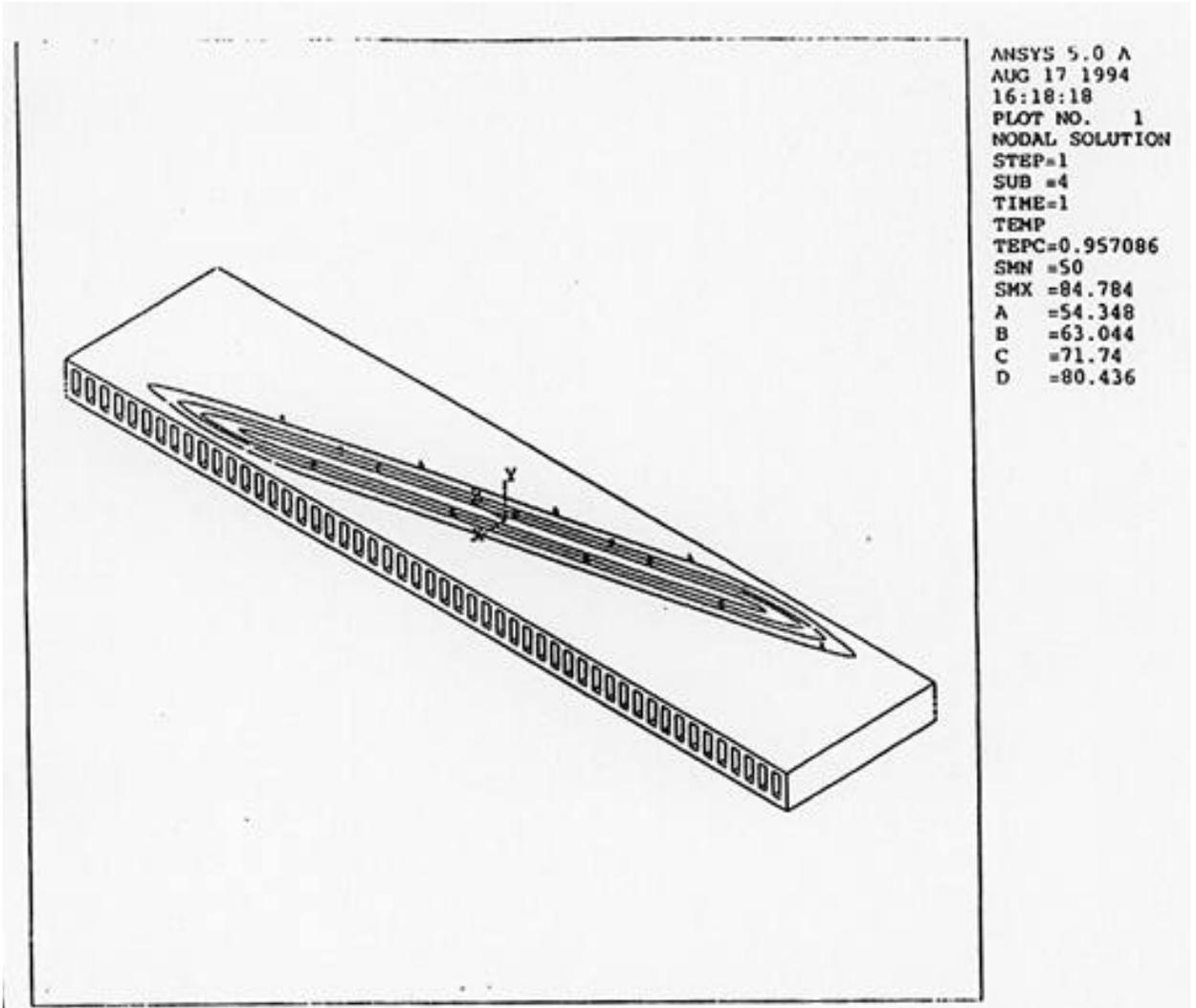
Fig. V.5: Temperature profile on the surface of a 78°-inclined crystal set to diffract 8 keV photons from undulator A beam at K = 1.235. The horizontal slit opening was set to 3.6 mm, while the vertical slits were left wide open. SMX and SMN are the maximum and the minimum temperatures, respectively.
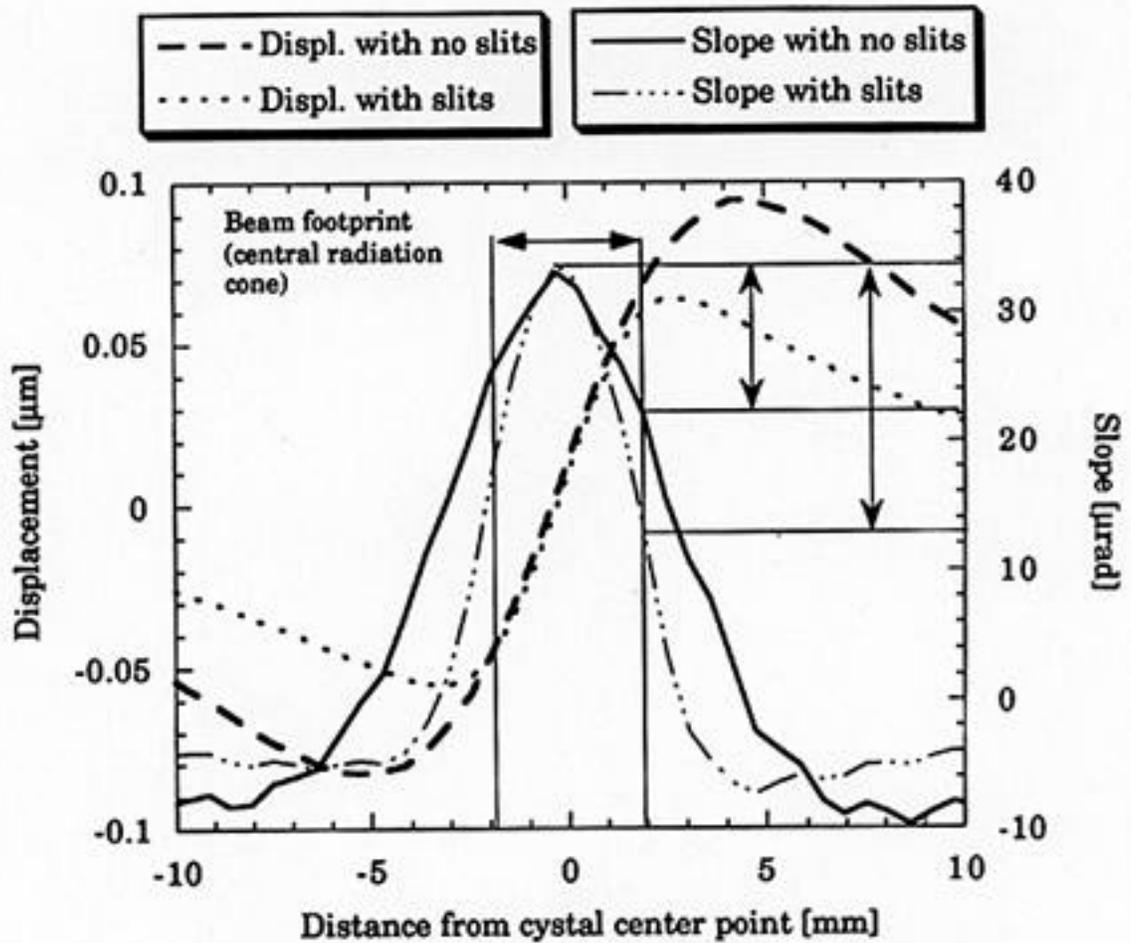
Fig. V.6: The inclined crystal: Displacement and thermally induced slope along the scattering plane for an 85° inclined Si(111) crystal set to diffract the first harmonic at 4.2 keV; comparison is made between the case with vertical slits (with 1.8 mm opening) and the case with no vertical slits; the horizontal slits are kept at 3.6 mm in all cases. The crystal and the slits are assumed to be located at 30 m from the source. This figure also indicates the beam footprint (4 x   of the central radiation cone/sin) and the differential slopes.
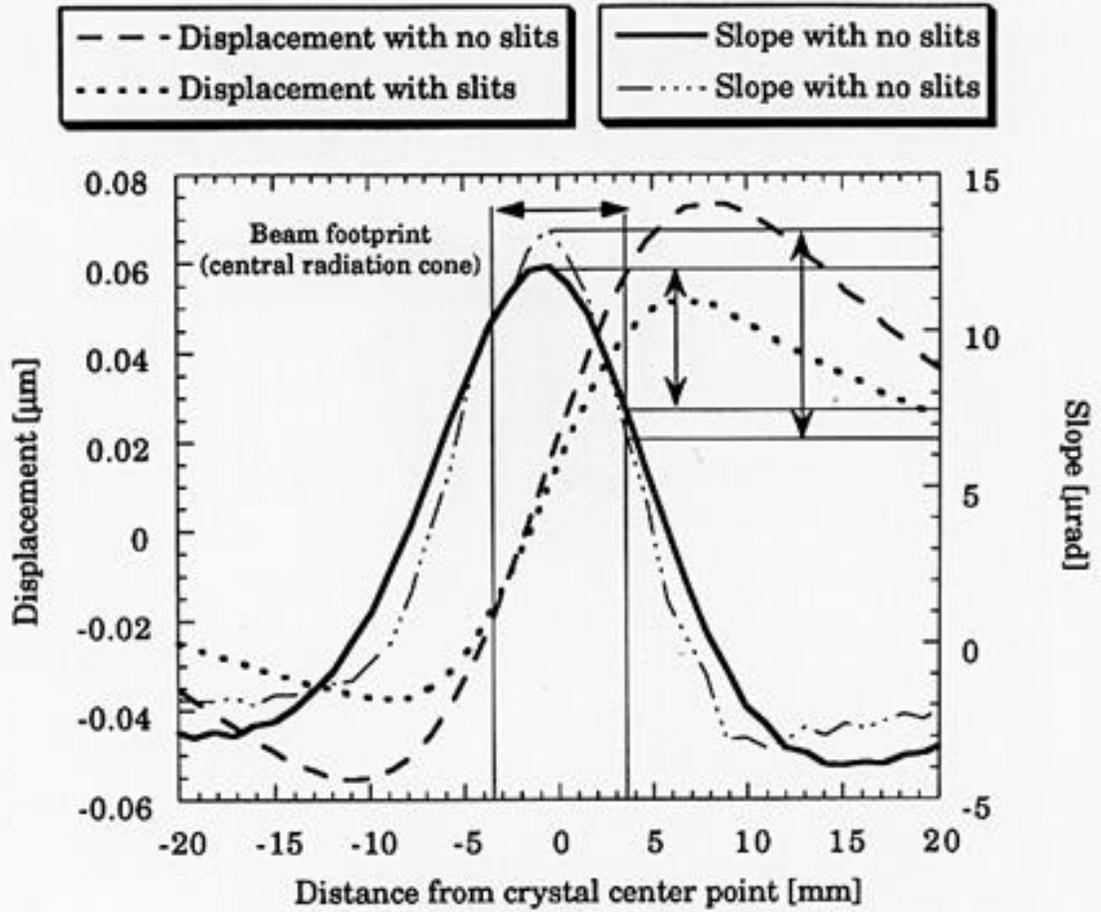
Fig. V.7: The inclined crystal: Displacement and thermally induced slope along the scattering plane for a 78° inclined Si(111) crystal set to diffract the first harmonic at 8 keV; comparison is made between the case with vertical slits (with 1.8 mm opening) and the case with no vertical slits; the horizontal slits are kept at 3.6 mm in all cases. The crystal and the slits are assumed to be located at 30 m from the source. This figure also indicates the beam footprint (4 x of the central radiation cone/sin) and the differential slopes.

VI. Experimental Results

This section summarizes our experimental results from various high-heat-load tests at CHESS and BNL. Fig. VI.1 shows the results of our first inclined crystal run at CHESS in September 1991 [33] using the CHESS/ANL undulator. The crystals had slots of about 1 mm wide and 3 mm deep, separated by about 1 mm. The bottom of the slots was about 0.8 mm from the surface of the crystal. Liquid gallium was used as a coolant. Details can be found in the reference. In the setup, the maximum normal incidence power density at the crystal at 100 mA ring current was about 32 W/mm^2. As can be seen from the figure, in the case of the flat crystal, the point at which a 10% loss in intensity occurs is at about 30 mA ring current. At 23.3° Bragg angle (5 keV Si(111)), this corresponds to a surface power density of about 3.8 W/mm^2. In the inclined crystal case, with a spreading by a factor of 3 over the flat crystals, the 10% loss point moved correspondingly upwards in current by nearly the same factor to 80 mA.

Another test of the inclined geometry was performed at the X-25 focused beamline at the NSLS in September 1991 [34]. In this case, the normal incidence power density was about 120 W/mm^2 at the crystal position, and the total power was about 38 W. A set of 85° inclination crystals was used. At a Bragg angle of 23.3° (Si(111), 5 keV), no thermal distortions were observed. At such an angle, the beam spreads across the surface of the crystal by a factor of 29, thus the surface power density was about 4.1 W/mm^2.

Our most recent high-heat-load experiment was done at CHESS in September 1993, again using the CHESS/ANL undulator. One of the results is shown in Fig. VI.2. In this setup, the normal incidence power density on the crystal at 100 mA was 23 W/mm^2. (We are further from the source as compared to the previous run.) In this case, using another slotted crystal of about the same dimensions as before, in the flat geometry, we see that the 10% loss in intensity occurs at about 50 mA ring current, which, at this Bragg angle, corresponds to about 4.5 W/mm^2.

These three independent experiments suggest to us that, by using the slotted-crystal geometry and liquid gallium as a coolant, we can handle about 4 W/mm^2 surface power density on the crystal. Keep in mind, however, that the total power involved in these tests was only about 300 to 400 watts at CHESS and only about 40 watts on X-25 at NSLS. At closed gap of the APS undulator A at 30 m, the central cone contains about 750 watts, and the total power of the wiggler is about 7 kW. Nevertheless, we see that our experimental numbers agree quite well with the FEA results. Fig. IV.5 shows that, for the APS wiggler beam, a surface power density of about 4 W/mm^2 would result in about a 5 µrad thermal distortion on the crystal. This is consistent with our measurements. Currently, we are not able to detect distortions less than about 5 µrad due to the residual strains in our crystals from the fabrication and/or mounting process.
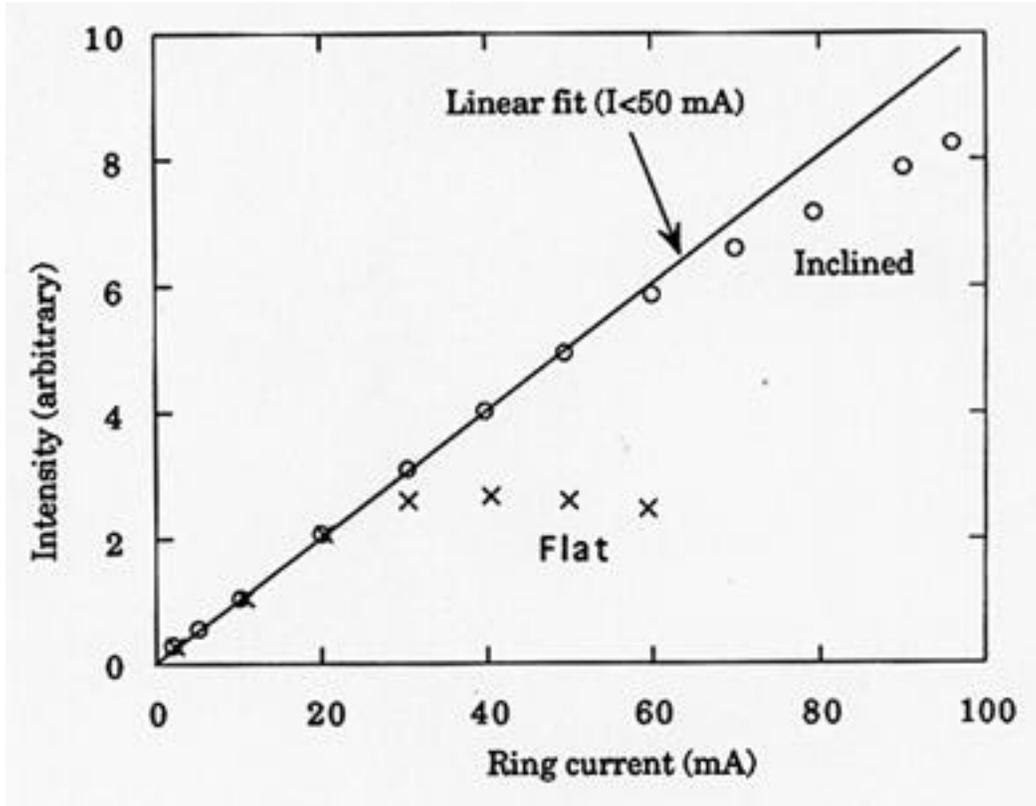
Fig. VI.1: Plot of intensity versus CESR current for a flat and an inclined crystal. The crystal had slots with liquid gallium as coolant. Data taken in June 1991 on the CHESS/ANL undulator. The inclined crystal data were taken by rotating the flat crystal 70.5° and using the (1, 1, -1) reflection. A straight line fit to the inclined crystal data for I < 50 mA is shown for reference. The advantage of the inclined crystal is clear. The 10% intensity loss occurs at about 30 mA for the flat crystal and at about 70 mA for the inclined crystal.
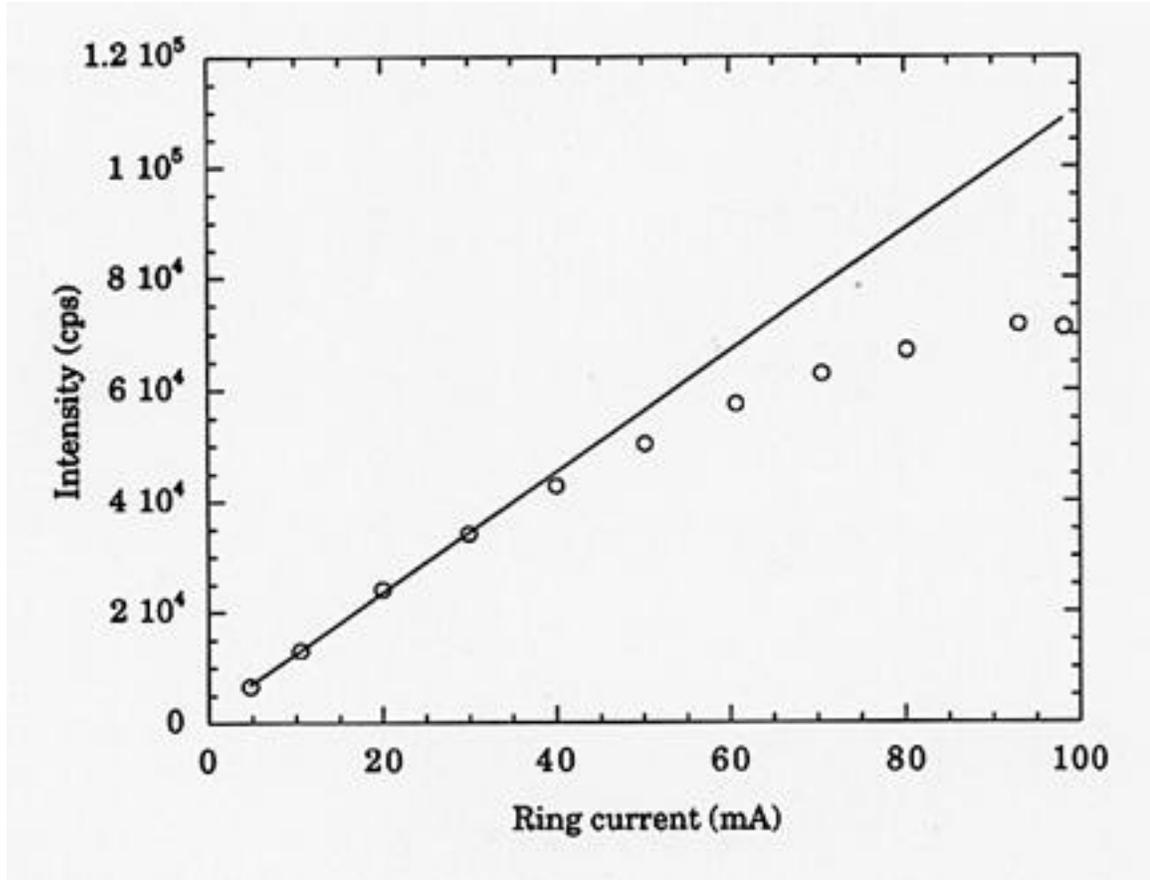
Fig. VI.2: Plot of intensity versus CESR ring current for a flat, slotted, and liquid-gallium-cooled crystal. Data taken in September 1993 on the CHESS/ANL undulator. The straight line is a linear fit to the I   30 mA data. The 10% intensity loss occurs at about 50 mA.

VII. Acknowledgment

VIII. References

1. R. K. Smither, G. A. Forster, C. A. Kot, and T. M. Kuzay, Nucl. Instrum. Methods A **266** (1998) 517.

2. R. K. Smither, G. A. Forster, D. H. Bilderbak, M. Bedzyk, K. Finkelstein, C. Henderson, J. White, L. E. Berman, P. Stefan, and T. Oversluizen, Rev. Sci. Instrum. **60** (1989) 1486.

3. R. K. Smither, W.-K. Lee, A. Macrander, D. Mills, and S. Rogers, Rev. Sci. Instrum. **63** (1992) 1746.

4. S. Rogers, D. Mills, and L. Assoufid, "The Cryogenic Cooling Program at the Advanced Photon Source," ANL/APS/TRB-18 (1994).

5. C. S. Rogers and L. Assoufid, to be published in Rev. Sci. Instrum.

6. W.-K. Lee and D. Mills, "High Heat Load Monochromator Specifications," Argonne National Laboratory Report ANL/APS/TB-4 (1993).

7. M. Khounsary, Rev. Sci. Instrum. **63** (1992) 461.

8. T. Macrander, W.-K. Lee, R. K. Smither, D. M. Mills, C. S. Rogers, and A. M. Khounsary, Nucl. Instrum. Methods A **320** (1992) 188.

9. W.-K. Lee, A. T. Macrander, D. M. Mills, C. S. Rogers, and R. K. Smither, Nucl. Instrum. Methods A **320** (1992) 381.

10. T. Macrander and W.-K. Lee, Nucl. Instrum. Methods A **319** (1992) 155.

11. W.-K. Lee and A. T. Macrander, Nucl. Instrum. Methods A **319** (1992) 158.

12. T. Macrander, A. M. Khounsary, and Graham, SPIE Vol. **1739**, *High Heat Flux Engineering* (1992) 502.

13. R. K. Smither and P. B. Fernandez, "Asymmetric-cut Monochromator with Adjustable Asymmetry," to be published in Nucl. Instrum. Methods.

14. M. Khounsary, R. K. Smither, and S. Davey, SPIE Vol. **1739**, High Heat Flux Engineering (1992) 628.

15. L. Assoufid and D. Mills, "Finite Element Analysis of a Diamond Crystal Subjected to the APS Undulator A Beam," Thermal Management of X-ray Optical Components for Synchrotron Radiation Workshop at Argonne National Laboratory, as part of The International Conference on Synchrotron Radiation Instrumentation, Stony Brook, NY, USA (1994).

16. ANSYS - A General Purpose Finite Element Analysis Program, Rev. 5.0a, Swanson Analysis System, Inc., Houston, PA 15342.

17. R. Lyon, "Forced Convection Heat Transfer Theory and Experiments with Liquid Metals," USAEC Report ORNL-361, Oak Ridge National Laboratory (1949).

18. V. Gnielinski, Int. Chem. Eng. **16** (1976) 359.

19. S. Petukhov, *Heat Transfer*, T. F. Irvine and J. P. Hartnett, eds., Vol. **6** (Academic Press, NY, 1970) pp. 503-564.

20. *Thermophysical Properties of Matter*, Vol. **2** *Thermal Conductivity*, Y. S. Toukoulian, R. W. Powell, C. Y. Ho, P. G. Klemens, eds. (IFI/Plenum, 1970) and Vol. **13** *Thermal Expansion*, Y. S. Toukoulian, R. K. Kirby, R. E. Taylor, and T. Y. Lee, eds. (IFI/Plenum, 1979).

21. G. K. Shenoy, P. J. Viccaro, and D. Mills, "Characteristics of the 7-GeV Advanced Photon Source: A Guide for Users," Argonne National Laboratory Report ANL-88-9 (1988).

22. T. Oversluizen, T. Matsushita, T. Ishikawa, P. M. Stefan, S. Sharma, and A. Mikuni, Rev. Sci. Instrum. **60** (1989) 1493.

23. J. Dejus, A. M. Khounsary, D. A. Brown, and P. J. Viccaro, Nucl. Instrum. Methods A **319** (1992) 207.

24. T. W. Tonnessen and J. Arthur, SPIE Vol. **1739**, *High Heat Flux Engineering* (1992) 622

25. J. Arthur, W. H. Tompkins, C. Troxel, R. J. Contolini, E. Schmitt, D. H. Bilderbak, C. Henderson, J. White, and T. Settesten, Rev. Sci. Instrum. **63** (1991) 433.

26. R. A. Riddle, SPIE Vol. **1997**, *High Heat Flux Engineering II* (1993) 83.

27. M. Kuzay, J. T. Collins, A. Khounsary, and J. Viccaro, SPIE Vol. **1345**, *Advanced X-ray/EUV Radiation Sources and Applications* (1990) 55.

28. Lai, A. Khounsary, R. Savoy, L. Moog, and E. Gluskin, "Wiggler A Characteristics and Specification," Argonne National Laboratory Report ANL/APS/TB-11 (1993).

29. F. Cerrina, B. Lai, K. Chapman, C. Welnak, and P. Runkle, Center of X-ray Lithography, University of Wisconsin.

30. Yun, A. M. Khounsary, B. Lai, and E. Gluskin, "Use of a Mirror as the First Optical Component for Undulator Beamlines at the APS," Argonne National Laboratory Report ANL/APS/TB-2 (1992).

31. R. J. Dejus, B. Lai, E. R. Moog, and E. Gluskin, "Undulator A Characteristics and Specification: Enhanced Capabilities," Argonne National Laboratory Report ANL/APS/TB-17 (1994).

32. R. P. Walker and B. Diviacco, Rev. Sci. Instrum. **63** (1992) 392.

33. T. Macrander, W.-K. Lee, R. K. Smither, D. M. Mills, C. S. Rogers, and A. M. Khounsary, Nucl. Instrum. Methods A **319** (1992) 188.

34. W.-K. Lee, A. T. Macrander, D. M. Mills, C. S. Rogers, and R. K. Smither, Nucl. Instrum. Methods A **320** (1992) 381.